

Increased RNA and protein degradation is required for counteracting transcriptional burden and proteotoxic stress in human aneuploid cells

Marica Rosaria Ippolito^{1,*}, Johanna Zerbib^{2,*}, Yonatan Eliezer², Eli Reuveni², Sonia Viganò¹, Giuseppina De Feudis¹, Eldad D. Shulman³, Anouk Savir Kadmon², Rachel Slutsky², Tiangen Chang³, Emma M. Campagnolo³, Silvia Taglietti¹, Simone Scorzoni¹, Sara Gianotti¹, Sara Martin¹, Julia Muenzner⁴, Michael Müllleder⁵, Nir Rozenblum², Carmela Rubolino⁶, Tal Ben-Yishay^{2,7}, Kathrin Laue², Yael Cohen-Sharir², Ilaria Vigorito¹, Francesco Nicassio⁶, Eytan Ruppin³, Markus Ralser^{4,8,9}, Francisca Vazquez¹⁰, Stefano Santaguida^{1,11,#}, Uri Ben-David^{2,#}

¹ Department of Experimental Oncology at IEO, European Institute of Oncology IRCCS, Milan, Italy

² Department of Human Molecular Genetics and Biochemistry, Faculty of Medicine, Tel Aviv University, Tel Aviv, Israel

³ Cancer Data Science Laboratory, Center for Cancer Research, National Cancer Institute, National Institutes of Health, MD, USA

⁴ Charité Universitätsmedizin Berlin, Department of Biochemistry, Berlin, Germany

⁵ Charité Universitätsmedizin Berlin, Core Facility High-Throughput Mass Spectrometry, Berlin, Germany

⁶ Center for Genomic Science of IIT@SEMM, Fondazione Istituto Italiano di Tecnologia, Milan, Italy

⁷ The Blavatnik School of Computer Science, Faculty of Exact Sciences, Tel Aviv University, Tel Aviv, Israel

⁸ Nuffield Department of Medicine, University of Oxford, Oxford, United Kingdom

⁹ Max Planck Institute for Molecular Genetics, Berlin, Germany

¹⁰ Broad Institute of MIT and Harvard, Cambridge, MA, USA

¹¹ Department of Oncology and Hemato-Oncology, University of Milan, Milan, Italy

* Equally-contributing first authors

Equally-contributing last authors

Running title: Aneuploid cells depend on RNA and protein metabolism

Correspondence:

- Stefano Santaguida (Stefano.santaguida@ieo.it, +39294375074, Department of Experimental Oncology, European Institute of Oncology, Via Adamello 16, 20139 Milan, Italy)
- Uri Ben-David (ubendavid@tauex.tau.ac.il, +972733804729, Faculty of Medicine Room 728, Tel Aviv University, POB 39040, Ramat Aviv, Tel Aviv 69978, Israel)

Conflict of interest: U.B.-D. received grant funding from Novocure, and receives consulting fees from Accent Therapeutics. E.Ruppin is a co-founder of MedAware, Meabomed and Pangea Biomed (divested), and an unpaid member of Pangea Biomed's scientific advisory board. F.V. receives research support from the Dependency Map Consortium, Riva Therapeutics, Bristol Myers Squibb, Merck, Illumina, and Deerfield Management. F.V. is on the scientific advisory board of GSK and holds equity and is a consultant for Riva Therapeutics and Jumble Therapeutics. The other authors declare no competing interests.

44 **Abstract**

45 Aneuploidy results in a stoichiometric imbalance of protein complexes that jeopardizes cellular
46 fitness. Aneuploid cells thus need to compensate for the imbalanced DNA levels by regulating their RNA
47 and protein levels, but the underlying molecular mechanisms remain unknown. Here, we dissected
48 multiple diploid vs. aneuploid cell models. We found that aneuploid cells cope with transcriptional burden
49 by increasing several RNA degradation pathways, and are consequently more sensitive to the perturbation
50 of RNA degradation. At the protein level, aneuploid cells mitigate proteotoxic stress by reducing protein
51 translation and increasing protein degradation, rendering them more sensitive to proteasome inhibition.
52 These findings were recapitulated across hundreds of human cancer cell lines and primary tumors, and
53 aneuploidy levels were significantly associated with the response of multiple myeloma patients to
54 proteasome inhibitors. Aneuploid cells are therefore preferentially dependent on several key nodes along
55 the gene expression process, creating clinically-actionable vulnerabilities in aneuploid cells.

56

57 **Statement of Significance**

58 Aneuploidy is a hallmark of cancer that is associated with poor prognosis and worse drug response. We
59 reveal that cells with extra chromosomes compensate for their imbalanced DNA content by altering their
60 RNA and protein metabolism, rendering them more sensitive to perturbation of RNA and protein
61 degradation.

62 **Introduction**

63 Aneuploidy is a genomic state characterized by chromosome gains and losses. A major
64 consequence of aneuploidy is genome and proteome imbalance, which aneuploid cells must overcome in
65 order to function properly. The degree of gene dosage compensation varies across different cellular
66 contexts(1), yet it is clear that in human aneuploid cancer cells the effect of aneuploidy is attenuated by
67 such buffering mechanisms. Recent studies have revealed that many proteins do not change their
68 expression by the degree expected based on their DNA levels(2–6). The mechanisms that allow for
69 dosage compensation, and the potential cellular vulnerabilities that result from them, remain under-
70 explored.

71 Previous studies have exposed the role of protein regulation and protein degradation for
72 “buffering” the effect of copy number alterations (CNAs). Aneuploid cells experience proteotoxic stress,
73 which is partly overcome in aneuploid yeast by an increased activity of the proteasome(7–10). Similarly,
74 a recent study described a protein folding deficiency in engineered aneuploid human cells(2). However,
75 the role of the proteasome in the context of aneuploid human cancer cells has remained unknown, and is
76 of particular clinical relevance given that proteasome inhibitors are used in the clinic (mostly for treating
77 multiple myeloma). It also remains unknown whether other important processes of protein metabolism,
78 such as protein translation, are also dysregulated in aneuploid cells.

79 Gene expression is also regulated at earlier stages of mRNA regulation. Whereas dosage
80 compensation at the mRNA level is minimal in yeast(7,11,12), it does occur in human cancer
81 cells(4,5,13). Recent analyses show that ~20% of genes in cancer cell lines and primary tumors do not
82 scale with chromosome-arm copy number levels(4,13). However, the potential role of RNA transcription,
83 metabolism and degradation in attenuating aneuploidy-induced gene expression changes – and whether
84 this can create cellular vulnerabilities in aneuploid cells – have yet to be explored.

85 In our companion study, we established a library of stable RPE1 clones with various degrees of
86 aneuploidy (14). Here, we analyzed genomic and functional data from these isogenic clones and
87 uncovered an increased vulnerability of aneuploid cells to perturbation of RNA and protein degradation
88 pathways. These novel aneuploidy-induced functional dependencies were validated in human cancer cell
89 lines, and differential activity of these pathways was confirmed in primary human tumors. These findings
90 may thus have important clinical ramifications, both for the development of novel cancer therapeutics and
91 for predicting patients’ response to existing drugs.

92 **Results**

93

94 **Dosage compensation in trisomic cells occurs at both mRNA and protein levels**

95 To investigate dosage compensation in aneuploid cells, we used a novel isogenic system of non-
96 transformed chromosomally stable aneuploid cells, presented in detail in our companion study (14).
97 Briefly, we transiently treated RPE1-hTERT cells with the MPS1 inhibitor reversine to induce
98 chromosome mis-segregation and generate aneuploidy(15,16), single-cell sorted and karyotyped the
99 obtained clones (**Fig. 1a** and Zerbib *et al* (14)). RPE1-hTERT clones carry a chromosome 10q
100 amplification as a clonal event of the parental cell line. This event is therefore shared by all the RPE1
101 clones, and we termed the parental and the control clones as “pseudo-diploid”. We selected 7 clones with
102 increasing degrees of aneuploidy: three pseudo-diploid clones, RPE1-SS48, RPE1-SS31 and RPE1-SS77
103 (hereinafter SS48, SS31 and SS77, respectively), two clones carrying a single extra chromosome, RPE1-
104 SS6 and RPE1-SS119 (hereinafter SS6 and SS119, respectively), and two clones carrying multiple
105 trisomies, RPE1-SS51 and RPE1-SS111 (hereinafter SS51 and SS111, respectively). We identified a p53-
106 inactivating mutation in the SS77 clone (14), and therefore used it as a *TP53*-mutant control, whereas the
107 SS48 and SS31 clones were used as *TP53*-WT pseudo-diploid controls throughout the study. We
108 characterized the clones extensively, demonstrating their high relevance for aneuploidy research(14).

109 We first investigated the gene expression differences between the pseudo-diploid and aneuploid
110 RPE1 clones, using genome-wide RNA sequencing (RNAseq) and mass-spectrometry-based proteomics.
111 As our aneuploid RPE1 clones harbor different trisomies, we then applied gene set enrichment analysis
112 (GSEA(17)) to identify gene expression signatures that are induced by aneuploidy regardless of the
113 specific affected chromosome(s). We found upregulation of signatures associated with RNA and protein
114 regulation in aneuploid clones, both at the RNA and protein levels (**Fig. 1b-c, Supplementary Fig. 1a**
115 ,and **Supp. Table 1-3**). Specifically, we identified a significant upregulation of signatures related to RNA
116 metabolism and gene silencing, *e.g.* ‘nonsense mediated decay’ and ‘gene silencing by RNAs’ (**Fig. 1b-c,**
117 **Supplementary Fig. 1a**), and to the unfolded protein response (UPR) and protein degradation, *e.g.*
118 ‘IRE1 α activates chaperones’ and ‘E3-Ub ligases ubiquitinate target proteins’ (**Fig. 1b-c, Supplementary**
119 **Fig. 1a**). These results suggest global attenuation of gene and protein expression in the trisomic clones,
120 consistent with previous studies(3,4,18–20).

121 Therefore, we set out to evaluate dosage compensation at both the mRNA and protein levels.
122 Indeed, we found that the RNA and protein expression levels did not scale linearly with the DNA content
123 (**Fig. 1d-f**). Interestingly, the correlation between the DNA and protein content was lower than that
124 between the DNA and RNA content, in line with a greater degree of dosage compensation at the protein
125 level(4,18,20). Nonetheless, in contrast to a previous report in yeast(18), we also found evidence for
126 significant dosage compensation at the mRNA level (**Fig. 1d-f**). Genes that reside on gained
127 chromosomes and encode for proteins that participate in protein complexes exhibited more dosage
128 compensation, in comparison to genes that reside on the same chromosomes but do not belong to any
129 protein complex – the protein abundance of such genes scaled with their DNA content to a lesser degree
130 (**Fig. 1g** and **Supplementary Fig. 1b**). We conclude that dosage compensation is characteristic of
131 trisomic cells, and is particularly important for protein complexes.

132 Therefore, we set out to identify genes that are preferentially essential in aneuploid cells, using
133 genome-wide CRISPR/Cas9 screens of the isogenic RPE1 clones(14). Consistent with their gene
134 expression profiles, unbiased pre-ranked GSEA analysis revealed that aneuploid clones were more

135 dependent on mechanisms of RNA degradation, and in particular on genes related to gene silencing
136 through RNA processing and decay, including the nonsense-mediated decay (NMD) pathway, the miRNA
137 pathway, and gene splicing (**Fig. 1h**). Indeed, the increased levels of DNA damage that we identified in
138 the aneuploid clones(14) might result in an excessive number of abnormal transcripts, potentially
139 explaining why aneuploid cells would be more dependent on RNA processing and degradation.
140 Moreover, aneuploid clones were also more dependent on protein degradation via the proteasome (**Fig.**
141 **1h**), consistent with ongoing proteotoxic stress and the resultant accumulation of aberrant proteins (**Fig.**
142 **1b-c**). These findings were independent of the p53 status of the clones (**Supplementary Fig. 1c**).
143 Together, these results suggest that cells with extra chromosomes strongly rely on the downregulation of
144 their gene expression to compensate for their extra DNA content, both at the RNA and at the protein
145 level.

146 **Increased RNA synthesis and degradation in trisomic cells**

147 To explore dosage compensation in aneuploid cells, we first assessed RNA synthesis in the RPE1
148 clones. We focused on the most aneuploid clones, SS51 (trisomic for chromosomes 7 and 22) and SS111
149 (trisomic for chromosomes 8, 9 and 18), and quantified newly synthesized RNA using Ethynyl Uridine
150 (5-EU) incorporation. Indeed, nascent RNA was more abundant in highly-aneuploid clones, with the
151 highest synthesis levels found in the most aneuploid clone, SS111 (**Fig. 2a-b**). In line with these findings,
152 the total levels of extracted RNA were higher in the highly-aneuploid clones in comparison to pseudo-
153 diploid clones (**Fig. 2c**), consistent with previous studies showing the correlation between DNA and RNA
154 content in aneuploid cells(4,18,21). To assess whether increased RNA synthesis is an immediate
155 consequence of aneuploidy, we quantified the newly synthesized RNA in parental RPE1-hTERT cells
156 (hereinafter parental RPE1 cells) 72hrs following a pulse of reversine. Interestingly, reversine-treated
157 RPE1 cells also increased their nascent RNA levels (**Fig. 2d-e**), in agreement with the results obtained in
158 the stable aneuploid clones.

159 Despite increased transcription, our analysis revealed that more genes were downregulated than
160 upregulated in the highly-aneuploid clones, independently of p53 mutation status ($p < 0.001$;
161 **Supplementary Fig. 2a-b**). As multiple pathways of RNA degradation were elevated in the aneuploid
162 clones (**Fig. 1b-c**), we next investigated RNA degradation in the pseudo-diploid vs. highly-aneuploid
163 clones. Gene set enrichment analysis showed increased RNA catabolism in highly-aneuploid cells in
164 comparison to their pseudo-diploid counterparts (**Fig. 2f**). We therefore leveraged our global RNAseq
165 data to quantify RNA degradation in the samples using ‘DegNorm’, an algorithm developed to quantify
166 degraded RNA and remove its effect from RNAseq data analyses(22). We found a significant increase in
167 the RNA degradation index (a measure for RNA degradation levels) in the highly-aneuploid clones (**Fig.**
168 **2g**). Interestingly, degraded transcripts correlated with gene length, especially in the aneuploid clones
169 (**Supplementary Fig. 2c**). GSEA of the degraded genes between the pseudo-diploid and highly-aneuploid
170 clones revealed that transcripts related to the DNA damage response and to miRNA gene silencing were
171 less degraded in the aneuploid cells (**Supplementary Fig. 2d**), consistent with the activation of the
172 DDR(14) and of the miRNA machinery in aneuploid cells (as discussed below). Importantly, there was no
173 difference in overall transcript degradation between diploid and gained chromosomes in the highly-
174 aneuploid clones (**Supplementary Fig. 2e**), suggesting that the increased degradation was not
175 chromosome-specific. We validated the increased RNA degradation in aneuploid clones by running a gel
176 electrophoresis on the total RNA extracted from the clones and quantifying the resultant ‘smears’ (**Fig.**
177 **2h-i** and **Supplementary Fig. 2f-g**). We note that RNA degradation levels were highest in the most
178 aneuploid clone, SS111, which also exhibited the highest levels of RNA synthesis (**Fig. 2a-b**). To further

179 investigate RNA degradation rate in our system, we inhibited RNA synthesis using actinomycin D and
180 estimated the mRNA content of several transcripts with a short half-life. RNA synthesis inhibition
181 affected the mRNA levels of these genes more strongly in the highly-aneuploid clones (**Fig. 2j** and
182 **Supplementary Fig. 2h**), indicating a higher RNA degradation rate. Together, these findings indicate that
183 the increased DNA content in the aneuploid clones with extra chromosomes leads to increased
184 transcription, followed by a global increase in both RNA synthesis and RNA degradation, resulting in
185 higher RNA turnover in these cells.

186 Importantly, to confirm that the pathway enrichments found in our RNAseq data analysis were
187 not confounded by the increased levels of RNA degradation in the aneuploid clones, we repeated all
188 differential gene expression analyses after computationally removing the degraded transcripts. We were
189 able to recapitulate the enrichments for DNA damage response(14), RNA metabolism and protein
190 degradation signatures (**Supplementary Fig. 2i-l**). Interestingly, transcripts encoding for CORUM
191 protein complex members(23) were degraded significantly more than other transcripts (**Fig. 2k**), in line
192 with the increased dosage compensation observed for these proteins (**Fig. 1g**).

193 **Increased NMD activity and dependency in aneuploid cells**

194 Next, we assessed potential mechanisms of RNA degradation. The highly aneuploid clones, SS51
195 and SS111, exhibited elevated transcriptional signatures of the NMD pathway (**Fig. 1b-c**, **Fig. 3a** and
196 **Supplementary Fig. 3a**). Importantly, the NMD pathway was elevated in the aneuploid clones even
197 when the expression of genes that reside on the gained chromosomes was removed from the analysis
198 (**Supplementary Fig. 3b**), indicating that this transcriptional response is not directly due to any specific
199 copy number gain. Thus, we compared the NMD pathway activity between the highly-aneuploid and
200 pseudo-diploid clones. First, we estimated NMD activity by calculating a transcriptional signature score
201 of described NMD targets(24). We found a significant increase in this transcriptional score in the highly-
202 aneuploid clones (**Fig. 3b**), consistent with the gene set enrichment analysis (**Fig. 3a**). Next, we validated
203 this increased activity using an NMD pathway reporter system(25), which confirmed that under standard
204 culture conditions highly-aneuploid clones elevated their NMD pathway activity in comparison to their
205 pseudo-diploid counterparts (**Supplementary Fig. 3c**).

206 We then turned to investigate the dependency of aneuploid cells on the NMD pathway. The NMD
207 pathway was among the very top differential dependencies of aneuploid cells in the CRISPR screen (**Fig.**
208 **1h**), with many of its components ranking among the most differentially-essential genes (**Fig. 3c**).
209 Importantly, these results held true even when the p53-mutated SS77 clone was included in the analysis
210 (**Supplementary Fig. 1c** and **Supplementary Fig. 3d**), indicating that the increased dependency of
211 aneuploid cells on NMD is not simply due to p53 activation. To validate this dependency, we exposed the
212 RPE1 clones to pharmacological inhibitors of NMD, ouabain and digoxin(25), and found that the highly-
213 aneuploid clones SS51 and SS111 were significantly more sensitive to both drugs (**Fig. 3d** and
214 **Supplementary Fig. 3e-g**). The effect of ouabain on the cells was mostly cytostatic, as it delayed the cell
215 cycle of the treated cells but did not increase their apoptosis (**Supplementary Fig. 3h-i**). We then
216 investigated CASC3 (also known as MLN51, localized on chromosome 17), the top differentially-
217 essential core member of the NMD pathway, and a key regulator of NMD pathway activation(26). We
218 found that highly-aneuploid clones upregulated their CASC3 expression in comparison to their pseudo-
219 diploid counterparts (**Fig. 3e**). Moreover, CASC3 protein expression levels increased following reversine-
220 mediated aneuploidization of the parental RPE1 cells, and this increase was observed also in *TP53-KD*
221 and *TP53-KO* RPE1 cells, indicating a p53-independent mechanism (**Supplementary Fig. 3j-m**).

222 Aneuploid clones were significantly more sensitive to genetic CASC3 inhibition by siRNA, and the
223 degree of the response to CASC3 depletion was associated with the degree of aneuploidy (**Fig. 3f** and
224 **Supplementary Fig. 3n-q**). In addition, reversine-induced aneuploidization of the parental pseudo-
225 diploid RPE1 cells also rendered the cells more sensitive to CASC3 inhibition (**Fig. 3g** and
226 **Supplementary Fig. 4a**). This effect was not limited to RPE1 cells – we induced aneuploidy using
227 reversine in two additional near-diploid non-transformed cell lines (BJ-hTERT and IMR90) and in three
228 additional near-diploid cancer cell lines (CAL51, HCT116, and SW48). We found that aneuploidization
229 renders the cells sensitive to CASC3 depletion across cell lines (**Fig. 3h-i** and **Supplementary Fig. 4b**).
230 Finally, intrigued by previous observations showing that NMD could get activated by the DDR(27,28),
231 we found that DNA damage induction using etoposide increased CASC3 expression levels in parental
232 RPE1 cells (**Supplementary Fig. 4c-d**), providing a plausible mechanistic link between the increased
233 DNA damage observed in the aneuploid cells(14) and their increased expression of, and dependency on,
234 the NMD pathway. Together, these results confirm that aneuploidy increases cellular dependency on the
235 NMD pathway.

236 Lastly, we asked whether NMD activity and dependency are linked to high degree of aneuploidy
237 in human cancer cells. Gene expression analysis of hundreds of human cancer cell lines revealed that
238 RNA metabolism, and particularly RNA degradation through the NMD pathway, were strongly associated
239 with the proliferation capacity of highly-aneuploid cancer cell lines (but not with that of near-euploid
240 cancer cell lines) (see **Methods; Fig. 3j**). Moreover, analysis of CRISPR screens revealed that highly-
241 aneuploid cancer cells were significantly more dependent on multiple members of the NMD pathway,
242 including CASC3 and the core NMD effector UPF1 (**Fig. 3k-l** and **Supplementary Fig. 4e-h**). To
243 validate this finding in additional models, we depleted CASC3 in three representative near-diploid
244 (CAL51, HCT116, SW48) and three representative highly-aneuploid (MDA-MB-468, A101D, SH10TC)
245 cancer cell lines. Indeed, highly-aneuploid cancer cell lines were significantly more sensitive to CASC3
246 depletion (**Fig. 3m** and **Supplementary Fig. 4i**). Finally, we found a significant association between
247 aneuploidy levels and the NMD signature across human primary tumors as well (**Fig. 3n**). We conclude
248 that NMD activity and dependency are associated with a high degree of aneuploidy in cancer cells.

249 **Increased miRNA-mediated RNA degradation and altered gene splicing in aneuploid cells**

250 The NMD pathway was not the only RNA degradation pathway that came up in our unbiased
251 genomic and functional analyses. Gene set enrichment analysis showed significant enrichment for
252 signatures associated with gene expression silencing via small RNA pathways (**Fig. 1b-c** and **Fig. 4a**).
253 This enrichment was conserved when the genes expressed from the gained chromosomes were removed
254 from the analysis (**Supplementary Fig. 5a**). Importantly, genome-wide miRNA profiling of our
255 clones(14) revealed a significant overlap between downregulated mRNAs and the known targets of
256 miRNA that were upregulated in aneuploid clones (**Fig. 4b** and **Supplementary Fig. 5b**), confirming the
257 role of miRNAs in regulating mRNA expression in aneuploid clones. Additionally, GSEA of near-diploid
258 HCT116 cells treated with reversine also showed upregulation of miRNA pathway-related signatures,
259 (**Supplementary Fig. 5c**), emphasizing the generalizability of this association.

260 Similar to the NMD pathway, the miRNA pathway was among the top differentially-essential
261 pathways in aneuploid cells (**Fig. 1h** and **Fig. 4c**), with the hallmark miRNA pathway genes XPO5,
262 DICER1 and DROSHA scoring among the 20 most differentially-essential genes overall (**Fig. 4c**). As
263 DROSHA (localized on chromosome 5) is the most upstream core member of this pathway, we
264 investigated its activity and the sensitivity to its inhibition in the RPE1 clones. The highly-aneuploid

265 clones significantly increased DROSHA mRNA and protein expression (**Fig. 4d**, **Supplementary Fig.**
266 **5d**), and were significantly more sensitive to siRNA-mediated DROSHA depletion, in comparison to the
267 pseudo-diploid clones (**Fig. 4e** and **Supplementary Fig. 5d-g**). Aneuploid clones with a single trisomy
268 displayed an intermediate phenotype (**Fig. 4d** and **Supplementary Fig. 5d-g**). Reversine-induced
269 aneuploidization of additional near-diploid non-transformed (BJ-hTERT and IMR90) and cancer
270 (CAL51, HCT116, SW48) cell lines increased their sensitivity to DROSHA depletion (**Fig. 4f-g**,
271 **Supplementary Fig. 5h**), confirming the link between aneuploidy and DROSHA dependency.

272 In line with these findings, DROSHA was also significantly over-expressed in highly-aneuploid
273 human cancer cell lines compared to near-diploid ones (**Fig. 4h**). Comparing three near-diploid and three
274 highly-aneuploid cancer cell lines confirmed that highly-aneuploid cancer cell lines were more dependent
275 on DROSHA (**Fig. 4i** and **Supplementary Fig. 5i**). Aneuploid human cancer cell lines were more
276 dependent on various other members of the miRNA pathway, and in particular on core members of the
277 RNA-induced silencing complex, or RISC, such as PACT (also known as PRKRA) and TRBP (also
278 known as TARBP2) (**Supplementary Fig. 6a-b**). In line with these findings, the aneuploid RPE1 clones
279 were preferentially more sensitive to the depletion of PRKRA and TARBP2 (**Supplementary Fig. 6c-f**),
280 and aneuploidization increased the sensitivity to depletion of these genes in two additional near-diploid
281 non-transformed and three additional near-diploid cancer cell lines (**Supplementary Fig. 6g-l**).
282 Moreover, depletion of PRKRA and TARBP2 in three near-diploid and three highly-aneuploid cancer cell
283 lines further confirmed that highly-aneuploid cancer cells are more sensitive to the depletion of these
284 RISC complex partners (**Supplementary Fig. 6m-p**). Lastly, high degree of aneuploidy was significantly
285 associated with elevated expression of the miRNA pathway across human primary tumors as well (**Fig.**
286 **4j**). Together, these results suggest that miRNA-mediated gene silencing plays an important role in
287 regulating gene expression in aneuploid cells.

288 Notably, we observed that the aneuploidy-induced changes in RNA metabolism were not limited
289 to RNA degradation – RNA splicing was also among the most differentially-essential pathways in our
290 CRISPR screens (**Fig. 1h**). Examining splicing activity in our model system, we observed downregulation
291 of several splicing signatures in highly-aneuploid clones (**Supplementary Fig. 6q**). Splicing analysis of
292 RNAseq data confirmed a significant decrease in both 5' and 3' alternative splicing in the aneuploid
293 clones (**Supplementary Fig. 6r-s**). These findings align with the reported competitive interplay between
294 miRNA biogenesis and RNA splicing(29), underscoring the miRNA pathway's significance in aneuploid
295 clones.

296 We conclude that various aspects of RNA metabolism are altered in aneuploid cells, and propose
297 that these cells suffer from transcriptional burden that is offset by increased RNA degradation, making
298 them dependent on the increased activity of two major RNA degradation mechanisms: NMD and
299 miRNAs.

300 **Increased proteotoxic stress and reduced translation in aneuploid cells**

301 Proteotoxic stress has been reported to be associated with aneuploidy in both yeast(7–11) and
302 engineered aneuploid mammalian cells(2,21,30–32), leading to reduced protein translation and increased
303 protein degradation, which contributes to dosage compensation at the protein level. Indeed, we identified
304 ongoing proteotoxic stress in our aneuploid clones (**Fig. 1b-c** and **Supplementary Fig. 1a**). GSEA
305 analysis showed that highly-aneuploid clones, SS51 and SS111, upregulated gene expression signatures
306 of proteotoxic stress and protein degradation compared to the pseudo-diploid clone SS48(**Fig. 5a**). To

307 validate these results, we characterized the unfolded protein response (UPR) – the primary consequence
308 of proteotoxic stress – in the RPE1 clones. We investigated the three main branches of the UPR(33), and
309 detected the activation of all of them in highly-aneuploid clones: increased mRNA expression of the
310 active XBP1 and EDEM1, indicating elevated activity of the IRE1 α branch (**Fig. 5b**); increased mRNA
311 and protein levels of the chaperone GRP78 (also known as BiP), indicating elevated activity of the ATF6
312 branch (**Fig. 5b-d**); and increased protein levels of PERK and ATF4, and increased mRNA levels of
313 CHOP, indicating elevated activity of the PERK branch (**Fig. 5b-d**). These findings confirm the
314 aneuploidy-induced UPR signatures identified by our RNAseq and proteomics data analysis (**Fig. 1b-c**
315 and **Fig. 5a**), in line with the need for dosage compensation at the protein level (**Fig. 1e-g**). Next, we
316 functionally characterized the UPR in the cells by measuring the response of the isogenic cell lines to the
317 ER stress inducer, tunicamycin. In line with their higher basal level of ER stress, aneuploid clones were
318 significantly more resistant to UPR induction (**Fig. 5e** and **Supplementary Fig. 7a-b**). Further, parental
319 RPE1 cells became more resistant to tunicamycin following reversine exposure (**Fig. 5f**). We confirmed
320 this increased resistance to ER stress induction in additional non-transformed cell lines (BJ-hTERT and
321 IMR90), and additional near-diploid cancer cell lines (CAL51, HCT116, SW48), in which we induced
322 aneuploidy by MPS1 inhibition (**Fig. 5g-h**). Reversine-mediated aneuploidization of these models was
323 also associated with activation of multiple UPR markers (**Supplementary Fig. 7c-g**). We then turned to
324 another isogenic system of RPE1 cells and their aneuploid derivatives, RPTs(34). In this model, RPE1
325 cells have doubled their genomes following cytokinesis inhibition, resulting in chromosomal instability
326 and highly-aneuploid cells(34). RPT cells also exhibit resistance to ER stress induction using tunicamycin
327 (**Supplementary Fig. 7h**). Finally, RNAseq of near-diploid human colon cancer cells, HCT116, treated
328 with reversine, also revealed a significant enrichment for the UPR signature (**Supplementary Fig. 7i**),
329 showing the importance of this process in aneuploid cells to manage the increased protein load.

330 UPR activation in response to accumulation of misfolded proteins results in translation
331 attenuation(33). To investigate whether UPR attenuates translation in our model, we performed a
332 SUnSET puromycin incorporation assay(35). Puromycin incorporation significantly decreased in the
333 aneuploid clones (**Fig. 5i-j** and **Supplementary Fig. 7j-k**), confirming that global translation levels are
334 reduced in these cells. Importantly, synchronous progression in the G1 cell cycle stage of both pseudo-
335 diploid and highly-aneuploid clones (**Supplementary Fig. 7l**) confirmed reduced translation in the
336 highly-aneuploid clones, demonstrating that the reduced translation is not merely due to a slower
337 proliferation rate (**Supplementary Fig. 7m-n**). We also found that RPTs exhibited decreased levels of
338 global translation (**Supplementary Fig. 7o-p**), and that reversine-mediated aneuploidization of the
339 parental RPE1 cells resulted in a similar reduction in global translation (**Fig. 5k-l**), further demonstrating
340 that ER stress and reduced translation are an immediate consequence of aneuploidy. Interestingly, NMD
341 inhibition using ouabain resulted in proteotoxic stress, and its effect was significantly stronger in the
342 aneuploid clones than in their pseudo-diploid counterparts (**Supplementary Fig. 7q-r**), linking the
343 compensation mechanisms at the RNA and protein levels.

344 Finally, gene expression analysis of hundreds of human cancer cell lines showed a significant
345 enrichment for UPR in highly-proliferative highly-aneuploid cancer cell lines (**Fig. 5m**), in line with a
346 recent report(4). Moreover, a lineage-controlled pan-cancer analysis of The Cancer Genome Atlas
347 (TCGA) mRNA expression datasets revealed a significant elevation of the UPR gene expression signature
348 in highly-aneuploid tumors (**Fig. 5n**), consistent with a recent TCGA analysis that associated UPR with
349 copy number alterations in general(36). Therefore, we conclude that both non-transformed and cancerous
350 aneuploid cells suffer from proteotoxic stress and must develop compensatory mechanisms to overcome

351 it. One such mechanism is the reduction of the global translation levels, which may be partly responsible
352 for the protein-level dosage compensation observed in aneuploid cells(3,4,18,20,21).

353

354 **Increased proteasome activity and dependency in aneuploid cells**

355 Proteotoxic stress also leads to protein degradation through the ubiquitin-proteasome system(37).
356 Indeed, our transcriptional and proteomics analyses suggested protein degradation to be elevated in the
357 aneuploid clones (**Fig. 1b-c**), and the proteasome pathway was among the top differential dependencies of
358 aneuploid cells in the CRISPR screen (**Fig. 1h**). We therefore hypothesized that highly-aneuploid cells
359 increase their proteasome activity to overcome proteotoxic stress, and that this makes them more
360 vulnerable to proteasome inhibition. We validated the increased expression and activity of the proteasome
361 complex in the RPE1 models. The highly-aneuploid clones increased the expression of the proteasome
362 subunits (**Fig. 6a**), suggesting an increased proteasome activity in this model. Consistent with this
363 finding, the mRNA expression of the same proteasomal subunits were upregulated in RPT cells
364 (**Supplementary Fig. 8a**), and following reversine treatment of the parental RPE1 cells (**Supplementary**
365 **Fig. 8b**). Moreover, GSEA of reversine-treated HCT116 cells revealed that aneuploid HCT116 cells tend
366 to increase (albeit not significantly) their proteasome expression (**Supplementary Fig. 8c**). We confirmed
367 that the highly-aneuploid cells significantly upregulated the chymotrypsin-like activity of their
368 proteasome using the ProteasomeGlo assay, in the highly-aneuploid RPE1 clones (**Fig. 6b**), in the RPT
369 cells (**Supplementary Fig. 8d**), and in the parental RPE1 cells following reversine-induced
370 aneuploidization (**Supplementary Fig. 8e**). Interestingly, the increase in proteasome activity
371 corresponded well with the degree of overexpression of the proteasome subunits across all three model
372 systems. Together, these results suggest that aneuploid cells activate the proteasome system to increase
373 their protein degradation.

374 We then turned to investigate the dependency of aneuploid cells on the proteasome. Core
375 proteasomal subunits were among the top differentially-essential genes in the CRISPR screen (**Fig. 6c**), so
376 that aneuploid clones were significantly more sensitive to the perturbation of the 26S proteasome subunits
377 than the pseudo-diploid clone (**Supplementary Fig. 8f**). To validate this finding, we exposed the RPE1
378 clones to two proteasome inhibitors, bortezomib (a clinically-approved drug) and MG132. The highly-
379 aneuploid clones were significantly more sensitive to proteasome inhibition than their pseudo-diploid
380 counterparts (**Fig. 6d** and **Supplementary Fig. 8g-i**). Bortezomib treatment induced apoptosis, and the
381 proportion of apoptotic cells following treatment was much higher in the highly-aneuploid clones
382 (**Supplementary Fig. 8j**). Interestingly, the most aneuploid clone, SS111, exhibited the strongest
383 resistance to ER stress induction (**Fig. 5e**), the strongest proteasome subunit expression and activity (**Fig.**
384 **6a-b**), and the strongest sensitivity to proteasome inhibitors (**Fig. 6d** and **Supplementary Fig. 8i-j**),
385 further supporting the association between aneuploidy and these cellular responses.

386 Next, we asked whether proteasome activity and dependency are associated with a high degree of
387 aneuploidy in human cancer cells as well. Gene expression analysis of hundreds of human cancer cell
388 lines revealed increased gene expression of both the 20S and 19S proteasome subunits in highly-
389 aneuploid cancer cells (**Fig. 6e-f**). We assessed the activity of the proteasome by comparing
390 chymotrypsin-like activity in three cell lines with a low degree of aneuploidy and three cell lines with a
391 high degree of aneuploidy, and found higher proteasome activity in the aneuploid cell lines (**Fig. 6g**).
392 Moreover, genes associated with the proliferation capacity of highly-aneuploid, but not of near-euploid,
393 cancer cell lines were strongly enriched for proteasome signatures (**Fig. 6h**). Importantly, we found a

394 significant association between aneuploidy and the proteasome gene expression signature in the TCGA
395 dataset as well (**Fig. 6i**), suggesting that this association holds true in primary tumors. Together, these
396 results suggest an increased proteasome activity in highly-aneuploid cancer cells.

397 We then investigated the association between aneuploidy and proteasome dependency in human
398 cancer cells. Highly-aneuploid cancer cells were more dependent on genetic (shRNA-mediated) silencing
399 of both the 20S and 19S proteasome subunits (**Fig. 6j-k**) and more sensitive to its pharmacological
400 inhibition using bortezomib (**Fig. 6l**). Reversine-induced aneuploidization of two near-diploid non-
401 transformed cell lines (BJ-hTERT and IMR90) and three near-diploid cancer cell lines (CAL51, SW48
402 and HCT116) rendered four of the five cell lines more sensitive to bortezomib (**Fig. 6m-n**; note that the
403 fifth cell line, HCT116, was extremely sensitive to the drug to begin with). Next, we selected five
404 representative cancer cell lines with a low degree of aneuploidy and five representative cancer cell lines
405 with a high degree of aneuploidy(38), and compared their response to bortezomib. Indeed, highly-
406 aneuploid cancer cells were more sensitive to the proteasome inhibitor (**Fig. 6o** and **Supplementary Fig.**
407 **8k-m**). To confirm that proteasome dependency is indeed causally related to aneuploidy in cancer cells,
408 we assessed the response of 578 human cancer cell lines to bortezomib, using the PRISM barcoded cell
409 line platform(39). The response to bortezomib was evaluated either in the absence or in the presence of a
410 low dose (250nM) of reversine (see **Methods**). At this concentration, reversine had a mild effect on
411 proliferation (**Supp. Table 4**), but significantly sensitized cancer cells to proteasome inhibition (**Fig. 6p**).
412 Therefore, we conclude that aneuploid cancer cells upregulate their proteasome activity in response to
413 proteotoxic stress, rendering them more sensitive to proteasome inhibition.

414 Finally, we assessed whether the degree of aneuploidy could indeed predict patients' response to
415 the FDA-approved drug bortezomib. We used gene expression data to infer the aneuploidy
416 landscapes(40,41) of multiple myeloma patients treated with bortezomib as a single agent(42), or in
417 combination with chemotherapies and with dexamethasone(43,44). Used as a single agent, we found that
418 within the immunoglobulin G myeloma subtype, the largest group in the dataset, the degree of aneuploidy
419 was significantly higher in patients that exhibited complete response (n=8) in comparison to patients who
420 experienced progressive disease (n=50; **Fig. 6q**). Used in combination with other drugs(43), the degree of
421 aneuploidy was also significantly higher in patients that exhibited complete response (n=13) in
422 comparison to patients who experienced progressive disease (n=14; **Fig. 6r**). This trend was conserved in
423 a third clinical dataset(44), in which multiple myeloma patients were treated with bortezomib in
424 combination with thalidomide and dexamethasone (VTD) (**Supplementary Fig. 8n**), albeit with
425 borderline significance due to the very low sample size of the 'non-responders' group (n=2). Finally, we
426 analyzed the response to proteasome inhibitors in pancreatic and pediatric PDX datasets. Response of
427 metastatic pancreatic cancer PDXs(45) to multiple proteasome inhibitors significantly correlated with
428 their aneuploidy score (**Supplementary Fig. 8o-q**). In addition, a linear regression analysis showed a
429 significant association between aneuploidy score and response to bortezomib in a panel of pediatric
430 PDXs(46) (**Supplementary Fig. 8r**). Together, these analyses suggest that the degree of aneuploidy is
431 clinically important for predicting the response of cancer patients to bortezomib (and, presumably, to
432 other proteasome inhibitors).

433 **Discussion**

434 **RNA metabolism in aneuploid cells**

435 Changes in gene copy number generally trigger corresponding changes in the amount of produced
436 mRNA(7–9,11,16,21,47,48). Accordingly, our data show that cells with gained chromosomes experience
437 increased RNA synthesis (**Fig. 2**). Importantly, we also found that trisomic cells upregulate pathways
438 involved in RNA degradation and gene silencing, and in particular the NMD and the miRNA pathways
439 (**Fig. 3** and **Fig. 4**). Buffering mechanisms might therefore attenuate the burden of an imbalanced
440 karyotype. Whereas protein dosage compensation has been reported to occur in aneuploid cells — in both
441 non-transformed(7–10,16,21,48,49) and cancer cells(4,5) – the role and impact of RNA metabolism in
442 dosage compensation is just emerging(19). Interestingly, dosage compensation at the mRNA level seems
443 to be minimal in yeast(12,18), but has been recently observed in human cells(4,6).

444 Intriguingly, the effect of extra chromosomes on RNA metabolism is not limited to the RNA
445 transcribed from the gained chromosomes, and is enriched for genes that encode for protein complex
446 members. In line with recent reports(5,6), we indeed found stronger dosage compensation at the protein
447 level, which was significantly enriched for protein complex members as well. How aneuploid cells evolve
448 to alter their global RNA metabolism in response to changes in gene dosage remains to be fully
449 understood. There are at least two possible scenarios: gene silencing might be the direct consequence of
450 increased gene expression, somehow sensed by the cells; or could be induced indirectly following
451 aneuploidy-induced cellular stresses. We favor the latter possibility and speculate that a major
452 aneuploidy-induced stress playing a role in this process is DNA damage. Indeed, the expression of the
453 NMD core component CASC3 increased following DNA damage in pseudo-diploid RPE1 cells,
454 consistent with previous reports of DDR-induced NMD activity(27,28). We propose that aneuploidy-
455 induced cellular stresses result in altered RNA metabolism in aneuploid cells, counteracting changes in
456 gene expression caused by imbalanced karyotypes.

457 Importantly, the increased dependency of aneuploid cells on RNA degradation was independent
458 of p53 status (**Supplementary Fig. 1-2**), indicating that this is a consequence of the aneuploid state *per*
459 *se*. We note, however, that our isogenic cell lines harbored extra chromosomes (trisomies), and the dosage
460 compensation mechanisms that we identify are therefore associated with trisomies rather than with
461 aneuploidy in general; different mechanisms for dosage compensation may be triggered upon
462 monosomy(4,50), and should be specifically addressed in future studies.

463 **Proteotoxic stress and proteasome dependency in aneuploid cells**

464 Tight control of pathways involved in protein translation and degradation is crucial to limit
465 proteotoxic stress in aneuploid cells(2,7–9,16,21,48,49). Proteotoxic stress is perhaps the most prominent
466 consequence of karyotype imbalances; the simultaneous overexpression of hundreds of genes on gained
467 chromosomes results in a massive burden on protein homeostasis. The effects of aneuploidy-induced
468 proteotoxic stress described so far are mainly: (a) overwhelming of the protein-folding machinery(2,30);
469 and (b) saturation of catabolic pathways responsible for the degradation of excessive proteins(9,16,21,30).
470 Importantly, our results indicate that aneuploid cells are sensing and responding to the altered demand for
471 the synthesis, folding and assembly of proteins both by attenuating global protein translation and by
472 reducing global protein degradation (**Fig. 5**), thereby “buffering” the stoichiometric imbalance induced by
473 aneuploidy.

474 Interestingly, protein buffering was recently reported to be common in cancer cells, suggesting
475 that maintenance of proper protein complex stoichiometries is crucial for tumor growth(28). A recent
476 TCGA analysis revealed that the abundance of proteasome subunits was correlated with the degree of

477 stoichiometric imbalance. Here, we took this notion further, demonstrating that aneuploid cancer cells not
478 only activate the proteasome but consequently become more dependent on its activity (**Fig. 6**). We show
479 that this association holds true in data from patient-derived xenografts and from human patients, and
480 propose that aneuploidy might be a biomarker for predicting tumor's response to proteasome inhibitors.

481 **The advantages and limitations of our datasets**

482 The combined analyses of mRNA, miRNA and protein expression data provides a comprehensive
483 framework for detailed analyses of dosage compensation in isogenic aneuploid RPE1 cells. Despite high
484 concordance among datasets, the statistical significance of proteomics data is lower than that of mRNA
485 data, most likely due to inherently higher technical variability in proteomics analyses. Furthermore, even
486 within each dataset, not all genes/proteins within a given pathway behave exactly the same. This is
487 expected, both due to the large-scale nature of these experiments, and due to biological differences across
488 genes/proteins (e.g., when a biological pathway is down-regulated, some genes in the pathway may be
489 overexpressed due to a feedback loop and compensatory mechanisms). For these reasons, we focused our
490 analyses of the profiling and screening data at the *pathway level*, using GSEA, and validated each
491 pathway by targeting multiple genes using multiple targeting approaches (e.g., multiple siRNAs to
492 knockdown a given gene, in order to reduce the off-target risk that is inherent to this type of perturbation).
493 Importantly, at the pathway level, the proteomic data analysis recapitulated very well all of the key
494 findings of the mRNA data analyses. Future integrative analyses of these datasets are therefore expected
495 to yield further insights into dosage compensation in aneuploid human cells.

496 **Concluding remarks**

497 Extensive transcriptome and proteome imbalance is one of the most immediate and important
498 consequences of aneuploidy. Our work indicates that RNA and protein metabolism – and in particular
499 their degradation – play a central role in attenuating the cellular impact of the increased DNA content that
500 inevitably characterizes trisomic cells. Therefore, dosage compensation might be achieved by
501 perturbation of various stages along the gene expression process (**Fig. 7**). Importantly, each of these
502 stages presents a potential opportunity for therapeutic intervention: cardiac glycosides might represent a
503 novel class of anti-aneuploid cancer therapeutics through targeting of NMD; and proteasome inhibitors
504 might be preferentially effective against aneuploid cancer cells due to their increased reliance on the
505 proteasome activity (**Fig. 7**). Those vulnerabilities might be further exacerbated by the ongoing CIN that
506 characterizes aneuploid cancer cells. As these drugs are already used in the clinic, clinical trials are now
507 necessary to determine if they can indeed be used to treat aneuploid tumors.

508 **Methods**

509 ***Cell culture***

510 RPE1-hTERT cells, their derivatives clones and RPT, CAL51, HCT116, SW48, EN, VMCUB, MDA-
511 MB-468 and A101D cell lines, were cultured in DMEM (Life Technologies) with 10% fetal bovine serum
512 (Sigma-Aldrich), 1% sodium pyruvate, 4mM glutamine, and 1% penicillin-streptomycin. BJ-hTERT was
513 cultured in DMEM supplemented with 10% fetal bovine serum, 4mM glutamine, 1% sodium Pyruvate,
514 0.01mg/mL hygromycin (Life Technologies) and 1% penicillin-streptomycin. IMR90 was cultured in
515 EMEM (ATCC) supplemented with 10% fetal bovine serum, 1% penicillin-streptomycin. SH10TC,
516 NCIH1693, MHHNB11 and PANC0813 were cultured in RPMI-1640 (Life Technologies) with 10% fetal
517 bovine serum (Sigma-aldrich) and 1% penicillin-streptomycin-glutamine (Life Technologies).
518 PANC0813 medium was supplemented with 10units/mL human recombinant insulin (Sigma-Aldrich),
519 and MHHNB11 medium was supplemented with MEM Non-Essential Amino Acids (Sigma-Aldrich).
520 Cells were cultured at 37°C with 5% CO₂ and are maintained in culture for maximum three weeks. All
521 cell lines were tested free of mycoplasma contamination routinely using Myco Alert (Lonza,
522 Walkersville, MD, USA) according to the manufacturer's protocol. All cell lines were kept in culture for
523 no more than 10 passages. Cell identification details are available in **Supplementary Table 5**.

524 The detailed generation and characterization of our isogenic aneuploid clones are described in our
525 companion study (14). Briefly, cells were seeded and synchronized with 5mM Thymidine for 24hrs, then
526 treated with 500nM reversine (or vehicle control) for 16hrs, then sorted, propagated and karyotyped.
527 Aneuploid RPE1 clones proliferate a bit slower than pseudo-diploid counterparts, but retain a similar
528 mitotic timing and a similar mitotic error rate.

529 To synchronize the RPE1 cells for protein translation assay, cells were seeded and treated with RO-3306
530 for 18hrs. Cells were released by 3-time PBS washes, then harvested 6hrs post-release.

531 To induce random aneuploidy, RPE1 cells were seeded and synchronized with 5mM Thymidine for
532 24hrs, then treated with 500nM reversine (or vehicle control) for 16hrs, BJ-hTERT and IMR90 were
533 treated with 500nM reversine for 36hrs, CAL51 and HCT116 were treated with 125nM reversine for
534 24hrs, and SW48 was treated with 200nM reversine for 24hrs. Drug and siRNA read-outs were performed
535 72hrs post reversine wash-out. UPR markers estimation was performed 24hrs post reversine wash-out.
536 For RNA-seq following reversine induction in the HCT116 cell line, cells were treated with 150nM
537 reversine for 72hrs before harvesting.

538

539 ***RNA synthesis***

540 Cells were seeded on coverslips coated with 5µg/ml fibronectin. 72hrs later, EZClick™ RNA label was
541 incubated for 1h at 37°C. Then, De novo synthesized RNA and DAPI were detected following
542 manufacturer's instructions. Coverslips were mounted using Mowiol. Cells were imaged using Leica SP8
543 confocal microscope with a magnification objective of 40x. FIJI software was used for the quantification
544 of nascent RNA spots area.

545

546 ***RNAseq and data analysis***

547 RNA sequence reads of RPE1 clones were obtained from Zerbib *et al* (14), and were analyzed as
548 previously described in Zerbib *et al*(14). Normalized read counts, and differential gene expression
549 analysis were generated using DESeq2 R package(51). GSEA and pre-ranked GSEA were performed on
550 the differentially expressed genes using GSEA software 4.0.3, with the following parameters: 1000
551 permutations and Collapse analysis, using the Hallmark, KEGG, Biocarta, and Reactome gene sets (in

552 separate analyses). Genes with fewer than 10 and 20 normalized read counts, for GSEA and pre-ranked
553 GSEA respectively, were excluded from further analyses.

554 GSEA was then performed on the modified gene expression matrix, as previously described. To control
555 for the copy number gains in the different RPE1 clones, genes localized on the gained chromosomes were
556 removed and the analysis was repeated.

557 Evaluation of degraded RNA was performed using 'DegNorm' with default parameters, as previously
558 described(22), to generate the degradation index (DI) and the degradation-free expression matrix. GSEA
559 was then repeated with the degradation-free expression matrix. Gene length was obtained from the
560 Ensembl BioMart database, and correlated to the degradation index. Pathway enrichment analysis of the
561 1% of genes that were most differentially degraded between the pseudo-diploid and highly-aneuploid
562 clones was performed using MSigDB.

563 NMD pathway transcriptional activity was evaluated as previously described(24). Briefly, we calculated
564 the R_{mRNA} score, i.e. the mRNA abundance of an NMD target gene, following the equation: $R_{mRNA} =$
565 $mE_{NMD}/\text{median_}mE_{non-NMD}$ (mE_{NMD} being the mRNA expression of the NMD target, and $\text{median_}mE_{non-}$
566 NMD being the median of mRNA expression of non-NMD target genes). To infer the NMD pathway
567 activity in aneuploid clones, an NMD transcriptional score, representing the relative abundance of the
568 NMD target gene in aneuploid clones compared to pseudo-diploid RPE1-SS48, was calculated following
569 the equation: $NMD\ score = R_{mRNA}(\text{aneuploid})/R_{mRNA}(SS48)$.

570 Differential splicing analysis was performed using VAST-Tool(52). RNAseq reads were aligned against
571 the VASTDB of the human reference genome hg19. The Percent Spliced-In (PSI) score for each splicing
572 event, representing the percentage of included splicing events out of total splicing events (higher the
573 index, lower the splicing activity), was calculated using the Vast-tool package and "compare" method,
574 between SS48 and each one of the aneuploid samples. Biological replicates were combined to enhance
575 read coverage and mitigate biased representation in alternative splicing events for highly expressed genes.
576 For the downstream analysis, only the alternative 3'/5' splice site events (Alt3, Alt5) with $PSI > 5$ were
577 considered.

578 For RNAseq of HCT116 cells, RNA was extracted from reversine-treated cells and from DMSO-control
579 cells, and RNA quality was assessed using TapeStation. RNA library was prepared using TruSeq Stranded
580 total RNA kit (Illumina) following manufacturer's protocol, and sequenced on Novaseq 6000 sequencer
581 (Illumina) following manufacturer's protocol. RNA sequence reads were aligned to the human reference
582 genome hg38 using STAR. Normalized counts and differential expression matrix of HCT116 following
583 reversine treatment were obtained using the 'DESeq2' R package. GSEA was performed on the
584 normalized expression matrix, as described above.

585

586 **Proteomics**

587 Proteomics was obtained and performed as previously described¹⁶. Briefly, samples were prepared from
588 1000 cells, incubated for 5 min at 95°C while shaking, and digested at 37°C for 17 hrs. Liquid
589 chromatography-Mass Spectrometry (LC-MS) followed by data independent acquisition (DIA) was
590 performed on an Evosep One system coupled to a Bruker timsTOF Pro 2 mass spectrometer, running
591 DIA-PASEF. Raw data were processed using DIA-NN 1.8.1(53) (<https://github.com/vdemichev/DiaNN>).
592 Human reference proteome from UniProt(54) was used for peptide and protein annotation (UP00000564,
593 downloaded 20230327). Raw data are available on the PRIDE database under accession number
594 PXD048833, output table is available in Zerbib *et al*(14). Gene set enrichment analysis (GSEA) was
595 performed as described in the RNAseq section.

596

597 **Dosage compensation and protein complexes analyses**

598 mRNA expression and protein abundance of each gene was normalized to the average expression of
599 genes residing on the diploid chromosomes of each clone, excluding chromosome 10, following the
600 method of Muenzner *et al*(18). Bottom 30% least expressed genes were excluded to reduce the noise from
601 the lowly expressed genes in the analysis. Results were plotted on a density plot in log2 scale, for both
602 mRNA and protein levels, and compared to expected DNA levels. To produce the line plot, averaged
603 expression (including genes residing on diploid and amplified chromosomes) of each clone was
604 calculated, and line equation was obtained using linear regression. The distance from the expected
605 equation (DNA content) and the mRNA and protein equations shows dosage compensation. All analyses
606 were performed using Seaborn, Matplotlib, and Scipy Python packages, statistical analysis was
607 performed using the Mann-Whitney test.

608 Genes and proteins implicated in the formation of protein complexes were identified using the CORUM
609 database(23). Expression of each gene (protein abundance or degradation index) was normalized to the
610 expression level in pseudo-diploid clone SS48. Results were plotted in a density plot, separating proteins
611 that are included or not in the CORUM protein complexes. For the proteomics, separated analysis for
612 genes localized on diploid and amplified chromosomes were performed. Statistical analysis was
613 performed using the Mann-Whitney test.

614 ***miRNA profiling***

616 miRNA profiling was obtained and performed as previously described in Zerbib *et al*(14). Briefly, small
617 RNA sequencing (sRNA-seq) library were prepared using 1000 ng of total RNA with the TruSeq Small
618 RNA Kit (Illumina), following the manufacturer's protocol. Sequencing was performed on an Illumina
619 Novaseq 6000 and sequencing quality was checked in the FASTQC report, and only experiments with
620 Q30 or above were considered (Phred Quality Score). Raw data together with detailed description of the
621 procedures are available in the GEO database under accession number GSE247267, and output table is
622 available in Zerbib *et al* (14).

623 To study the impact of miRNAs on mRNA expression, a list of differentially downregulated mRNA and
624 differentially upregulated miRNAs relative to SS48 were generated from the RNA-seq and miRNA-seq
625 data. To generate both lists, only the genes significantly ($qvalue \leq 0.25$) were differentially expressed
626 (\log_2 fold change ≥ 1) were included. Both lists were crossed to identify the downregulated mRNAs due
627 to the upregulated miRNAs. Venn diagrams and statistics were performed using Python.

628 ***Total RNA electrophoresis***

630 RNA was harvested from 1 million cells using Bio-TRI® (BioLabs) following the manufacturer's
631 protocol. RNA was run in 1% agarose gel in a cleaned chamber, and migration was imaged every 20min.
632 Smear quantification was performed using ImageJ, by quantifying the smear between the 28S and 16S
633 bands, relative to the total amount of RNA.

634 ***Genome-wide CRISPR screens and data analysis***

636 CRISPR dependency scores (CERES scores) were obtained from Zerbib *et al* (14). Dependency analysis
637 was performed as previously described in Zerbib *et al* (14), by a pre-ranked GSEA was on the
638 differentially-expressed genes using GSEA software 4.0.3, with the following parameters: 1,000
639 permutations and Collapse analysis, using the Hallmark, KEGG, Biocarta, and Reactome gene sets (in
640 separate analyses).

641 ***Dependency Map data analysis***

643 Extension of the aneuploidy scores (AS) table of each cancer cell line was obtained from Zerbib *et al*
644 (14). mRNA gene expression values, CRISPR and RNAi dependency scores (Chronos and DEMETER2
645 scores, respectively) were obtained from DepMap 22Q1 release
646 (https://figshare.com/articles/dataset/DepMap_22Q1_Public/19139906), and compared between the
647 bottom ($AS \leq 8$) and top ($AS \geq 21$) aneuploidy quartiles.

648 Doubling time (DT) analyses was performed as previously described in Zerbib *et al* (14). Briefly, using
649 the extended aneuploidy score table, and within the bottom ($AS \leq 8$) and the top quartile ($AS \geq 21$), DT of
650 each cancer cell line(55) was correlated to gene expression utilizing a linear model following the method
651 of Taylor *et al*(56). Genes were determined as overexpressed in highly proliferative aneuploid cancer
652 cells if they were significantly associated with DT within the top AS quartile but not within the bottom
653 AS quartile. Significance thresholds: ($\log_{10}(\text{p-value}) \geq 2.5$) OR ($-\log_{10}(\text{p-value}) \geq 1.3$ AND correlation
654 coefficient < -0.005). The resultant list of genes is available as a supplementary table in Zerbib *et al* (14).
655 This list was subjected to gene set enrichment analysis using the ‘Hallmark’, ‘KEGG’, ‘Reactome’ and
656 ‘Gene Ontology Biological Processes’ gene set collections from MSigDB ([http://www.gsea-](http://www.gsea-msigdb.org/gsea/msigdb/)
657 [msigdb.org/gsea/msigdb/](http://www.gsea-msigdb.org/gsea/msigdb/))(17,57).

658

659 ***qRT-PCR***

660 Cells were harvested using Bio-TRI® (Bio-Lab) and RNA was extracted following manufacturer’s
661 protocol. cDNA was amplified using GoScript™ Reverse Transcription System (Promega) following
662 manufacturer’s protocol. qRT-PCR was performed using Sybr® green, and quantification was performed
663 using the ΔCT method. To estimate RNA degradation rate, cells were treated with 5 $\mu\text{g/ml}$ actinomycin D
664 for 30’ for cJun, 1hr for EGR1 or 3hrs for KIF18a and PLK4, harvested with Bio-TRI®, and the mRNA
665 abundance was assessed for several mRNAs with a short half-life (cJUN, EGR1, KIF18A and PLK4). All
666 primer sequences are available in **Supplementary Table 5**.

667

668 ***NMD pathway reporter assay***

669 NMD pathway reporter assay was performed as previously described(25). Briefly, 300,000 cells were
670 seeded in 6-well plates and transfected 24hrs later with 2 μg of pBS-(CBR-TCR(PTC))-(CBG-TCR(WT))
671 plasmid(25) using *TransIT-LT1*® (Mirus, MIR2300), following manufacturer’s protocol. Medium was
672 replaced 24hrs post-transfection. 72hrs post-transfection, RNA was harvested from the treated cells using
673 Bio-TRI® (BioLabs) following the manufacturer’s protocol. RNA was cleaned from plasmid
674 contamination using TURBO DNA-free™ Kit (Invitrogen, AM1907) following the manufacturer’s
675 protocol. cDNA was amplified using GoScript™ Reverse Transcription System (Promega) following the
676 manufacturer’s protocol. qRT-PCR was performed using Sybr® green, and quantification was performed
677 as previously described(25).

678

679 ***Drug treatments***

680 Drug treatments were performed as previously described in Zerbib *et al* (14). Briefly, cells were seeded in
681 a 96w plate using Multidrop™ Combi Reagent Dispenser (ThermoFisher), then treated 24hrs later with
682 drugs of interest. Alternatively, following aneuploidy induction, cells were washed with PBS to remove
683 reversine and drugs were applied ~4hrs after seeding the cells. Cell viability was measured at indicated
684 time point using the MTT assay (Sigma M2128). Formazan crystals were extracted using 10% Triton X-
685 100 and 0.1N HCl in isopropanol, and color absorption was quantified at 570nm and 630nm. EC50 for
686 each drug was calculated using GraphPad PRISM 9.1, inhibitor vs. response (four parameters) non-linear
687 regression model.

688 Validation of bortezomib treatment was performed on 5 near-euploid (CAL51, EN, MHHNB11, SW48
689 and VMCUB1) and 5 highly aneuploid (MDA-MB-468, NCIH1693, PANC0813, SH10TC, A101D)
690 cancer cell lines. Cells were seeded in a 96w plate, and treated 24hrs later with various concentrations of
691 bortezomib. Cell viability was measured after 72hrs using CellTiter-Glo (Promega). EC50 was calculated
692 using GraphPad PRISM 8, asymmetric (five parameters) non-linear regression model. In **Supplementary**
693 **Fig. 8m**, CAL51 and MDA-MB-468 were imaged after 72hrs exposure to bortezomib, using Incucyte
694 (Satorius). For visualization, the cell borders were highlighted using AI-trained Ilastik® software. All
695 drug details are available in **Supplementary Table 5**.

696

697 *Flow cytometry analyses*

698 RPE1 clones were seeded and treated with 20nM ouabain or 2.4nM bortezomib for 48hrs. For cell death
699 assessment, cells were washed and live-stained with Annexin V/PI (#640930, BioLegend) following
700 manufacturer's protocol. For cell cycle, cells were fixed using ice-cold 70% ethanol for 2hrs on ice, then
701 stained with 50µg/mL Propidium Iodine (BioLegend) and 0.1mg/mL RNase A (Invitrogen) in PBS for
702 10min at RT. Flow cytometry acquisition was performed on CytoFLEX® (Beckman Coulter) and data
703 analysis was performed using CytExpert v2.4 analysis software (Beckman Coulter). The same gating of
704 live single cells was applied across all the analyzed samples, whereas gating of cell cycle phase was
705 specific to each clone.

706

707 *siRNA transfection*

708 Cells were transfected with siRNAs against CASC3 DROSHA, PRKRA, or TARBP2 (ONTARGETplus
709 SMART-POOL®, Dharmacon; individual oligos, Sigma-Aldrich), or with a control siRNA
710 (ONTARGETplus SMART-POOL®, Dharmacon; non-targeting siRNA, Sigma-Aldrich) using
711 Lipofectamine® RNAiMAX (Invitrogen) following manufacturers' protocols. To test whether aneuploidy
712 induction sensitized cells to CASC3, cells were seeded and synchronized with Thymidine 5mM for 24hrs,
713 then treated with reversine 500nM for 20hrs. After the reversine pulse, cells were reverse transfected with
714 siRNA against CASC3 using Lipofectamine® RNAiMAX following the manufacturer's protocol. Cell
715 growth following siRNA transfection was followed by live cell imaging using Incucyte® (Satorius). The
716 effect of the knockdown on viability was calculated by comparing the cell number in the targeted siRNA
717 vs. control siRNA wells at 72hrs post transfection. All oligo details are listed in **Supplementary Table 5**.

718

719 *Western blot*

720 Cells were lysed in NP-40 lysis buffer (1% NP-40;150mM NaCl; 50mM Tris HCl pH 8.0) with the
721 addition of protease inhibitor cocktail (Sigma-Aldrich #P8340) and phosphatase inhibitor cocktail (Sigma
722 Aldrich #P0044). Protein lysates were sonicated (Bioreactor) for 5min (30sec on/30sec off) at 4°C, then
723 centrifuged at maximum speed for 15 min and resolved on 12% SDS-PAGE gels. Bands were detected
724 using chemoluminescence (Millipore #WBLUR0500) on Fusion FX gel-doc (Vilber). For SUnSET
725 puromycin incorporation assay, cells were treated with 10µg/mL puromycin for 30min prior to harvest.
726 All antibodies are listed and their use is described in **Supplementary Table 5**.

727

728 *Proteasome activity assay*

729 Proteasome activity was estimated using Proteasome Glo® Chemotrypsin-like kit (Promega) following
730 manufacturer's protocol. Briefly, cells were trypsinized and washed twice with medium to remove
731 residual trypsin. 4,000 cells were seeded in triplicate in a white 96-well plate, and incubated for 2hrs at
732 37°C. 30min exposure to 1µM of bortezomib was used as a positive control for proteasome activity

733 inhibition. Plate was shaken for 2min at high speed, incubated for 5min at RT, and luminescence was then
734 measured using a Synergy H1 plate reader (BioTEK).

735

736 **PRISM screen**

737 PRISM screen was performed as previously described(38,39). Briefly, cells were plated in triplicate in
738 384-well plates at 1,250 cells per well. Cells were treated with the proteasome inhibitor bortezomib (8
739 concentrations of threefold dilutions, ranging from 91nM to 20μM) in presence of reversine (250nM) or
740 DMSO for 5 days. Cells were then lysed, and lysate plates were pooled for amplification and barcode
741 measurement. Viability values were calculated by taking the median fluorescence intensity of beads
742 corresponding to each cell line barcode, and normalizing them by the median of DMSO control. Dose-
743 response curves and EC50 values were calculated by fitting four-parameter curves to viability data for
744 each cell line, using the R drc package, fixing the upper asymptote of the logistic curves to 1. EC50
745 comparisons were performed on the 387 cell lines for which well-fit curves ($r^2 > 0.3$) were generated.

746

747 **TCGA data analysis**

748 TCGA data were retrieved using TCGAAbiolinks R package(58). Aneuploidy scores (AS) were obtained
749 from Taylor *et al*(56), and correlated to tumor gene expression using lineage as a covariate (lm function in
750 R studio v4.1.1, using the equation: gene~AS+lineage), as previously described(56). Genes were ranked
751 based on their aneuploidy score coefficient, and then subjected to pre-ranked gene set enrichment
752 analysis(17) using the ‘Hallmark’, ‘Biocarta’, ‘KEGG’, and ‘Reactome’ gene set collections from
753 MSigDB.

754

755 **Analyses of data from clinical trials**

756 Raw SNP6 CEL, gene expression and response data were obtained from the Gene Expression Omnibus
757 database for monotherapy(42) (GSE9782) or combination therapies(43,44) (GSE159426, GSE69028)
758 multiple myeloma clinical trials. For the monotherapy trial(42), the CAFE algorithm(41) v1.34.0 was
759 used to assess the chromosome-arm aneuploidy (CAA) score for each patient, with the armStats function
760 and default parameters were used to identify significant chromosome-arm losses and gains (Bonferroni
761 adjusted p-value<0.05). For the combination therapy trial GSE159426(43), gene expression was
762 quantified using Kallisto(59), and gene-level copy number variation (CNV) was inferred from the gene
763 expression using CNVkit(60). For the combination therapy trial GSE69028(44), the segmented copy
764 number calls for each patient were estimated using Rawcopy(61) v1.1 from the raw SNP6 CEL files,
765 using default parameters. For both combination therapy trials, aneuploidy scores were calculated using
766 ASCETS(62). For all clinical trials, the inferred aneuploidy scores were compared between the ‘non-
767 responders’ (Progressive Disease, Stable Disease, or Minimal Response) and the ‘responders’ (Complete
768 Response) patients.

769 Drug response data of the metastatic PDAC PDX cohort(45) was obtained from the EMBL-EBI database
770 (E-MAT-5039). Gene expression was quantified using Kallisto(59) and gene-level CNV was inferred
771 from the gene expression using CNVkit(60). Aneuploidy scores were calculated by calculating the
772 number of chromosome arms that deviate from basal ploidy using ASCETS(62), with a cut-off of
773 $|\log_2(\text{CNV})| > 0.3$. Drug response data from the pediatric PDX cohort was obtained (EA00001002528) and
774 tumors were separated based on their response to drugs of interest as previously described(46). Copy
775 number calling was performed using the CONserting algorithm(63), and kindly provided by Dr.
776 Jiyang Yu. Linear regression analysis to assess the relationship between the AUC (dependent variable)
777 and aneuploidy score (independent variable) was performed using the Statsmodel Python package.

778

779 **Statistical analyses**

780 The number of cells used for each experiment is available in the method section. Western Blot
781 quantifications were performed using ImageJ® and Image Lab. The numbers of independent experiments
782 and analyzed cell lines of each computational analysis are available in the figure legends. Statistical
783 analyses were performed using GraphPad PRISM® 9.1. Details of each statistical test are indicated in the
784 figure legends. In each presented box plot, the internal bar represents the median of the distribution. In
785 **Fig. 1c** and **Fig. 1f**, the bar represents the mean \pm SEM. Significance thresholds were defined as p-value
786 = 0.05 and q-value = 0.25.

787 **Materials availability**

788 Aneuploid RPE1-hTERT clones generated in this study are available upon request to Stefano Santaguida.
789 Raw RNAseq data are available in the SRA database (<https://www.ncbi.nlm.nih.gov/sra>) under accession
790 number PRJNA889550 (RPE1-hTERT clones) or PRJNA1097018 (aneuploidy-induced HCT116).
791 miRNA sequencing data and proteomics of RPE1-hTERT clones are available in the GEO database
792 (GSE247267) and the PRIDE database (PXD048833), respectively. Genome-wide CRISPR/Cas9
793 screening data of RPE1-hTERT clones are available in the DepMap database 21Q3 release
794 (https://figshare.com/articles/dataset/DepMap_21Q3_Public/15160110). Cancer cell line expression,
795 CRISPR/Cas9 and RNAi data are available in the DepMap database 22Q1 release
796 (https://figshare.com/articles/dataset/DepMap_22Q1_Public/19139906). Aneuploidy scores of cancer cell
797 lines are available in Zerbib *et al* (14).

798 **Acknowledgments**

799 The authors would like to thank James McFarland and Ofir Hameiri for their bioinformatic support; Gil
800 Ast, Marina Mapelli, Zuzana Tothova and members of the Ben-David and Santaguida labs for helpful
801 discussions; Varda Wexler for assistance with Figure preparation; Zuzana Storchova for providing the
802 RPE1/RPT cell lines; Zhongsheng You for providing the NMD reporter constructs; and Nicholas Lyons,
803 Jordan Bryan, Samantha Bender and Jennifer Roth for their assistance with the PRISM screen. We thank
804 the Broad Institute Genomic Perturbation Platform for their assistance with the CRISPR/Cas9 screens.
805 This work was supported by the European Research Council Starting Grant (grant #945674 to U.B.-D.),
806 the Israel Cancer Research Fund Project Award (U.B.-D.), the Azrieli Foundation Faculty Fellowship
807 (U.B.-D.), the DoD CDMRP Career Development Award (grant #CA191148 to U.B.-D.), the Israel
808 Science Foundation (grant #1805/21 to U.B.-D.), the BSF project grant (grant #2019228 to U.B.-D.), the
809 Italian Association for Cancer Research (AIRC-MFAG 2018 - ID. 21665 and Bridge Grant 2023 - ID.
810 29228 projects to S.S.), Ricerca Finalizzata (GR-2018-12367077 to S.S.), Fondazione Cariplo (S.S.), the
811 Rita-Levi Montalcini program from MIUR (to S.S.) and the Italian Ministry of Health with Ricerca
812 Corrente and 5x1000 funds (S.S.). U.B.-D. is an EMBO Young Investigator. J.Z. was supported by
813 fellowships from the Israeli Ministry for Immigrant Absorption, the Pfizer-Wexler Excellence
814 Scholarship, and the Yoran Institute for Human Genome Research, and by travel awards from the TAU
815 Constantiner Institute and Cancer Biology Research Center. M.R.I. is supported by an AIRC Fellowship
816 (ID 26738-2021). J.Z., R.S. and Y.E are PhD and MD-PhD students within the graduate school of the
817 Faculty of Medicine, Tel Aviv University. T.B.-Y. was supported in part by a fellowship from the
818 Edmond J. Safra Center for Bioinformatics at Tel Aviv University. M.R.I., S.M, S.V. and S.S. are PhD
819 students within the European School of Molecular Medicine (SEMM).

820 **Author contributions**

821 U.B.-D. and S.S. jointly conceived the study, directed and supervised it. J.Z. and M.R.I. jointly designed
822 and performed most of the experiments. J.Z., M.R.I., U.B.-D. and S.S. analyzed the data with inputs from
823 all co-authors. Y.E. and E.Reuveni, E.S, T.C., E.C., T.B.-Y. and E.Ruppin assisted with bioinformatic
824 analyses. S.V., G.D.F., A.S.K., R.S., S.T., S.S., S.G., S. M, K.L., J.M., M.M. N.R., F.N., M.R., Y. C.-S.
825 and I.V. assisted with *in vitro* experiments. F.V. directed the genomic profiling and CRISPR screens. J.Z.,
826 M.R.I., U.B.-D. and S.S. wrote the manuscript with inputs from all co-authors.

827 **Corresponding authors**

828 Further information and requests for resources and reagents should be directed to and will be fulfilled by
829 Uri Ben-David (ubendavid@tauex.tau.ac.il) and Stefano Santaguida (stefano.santaguida@ieo.it).

- 831 1. Kojima S, Cimini D. Aneuploidy and gene expression: is there dosage compensation?
832 Epigenomics 2019;11:1827–37.
833
- 834 2. Donnelly N, Passerini V, Dürrbaum M, Stingle S, Storchová Z. HSF 1 deficiency and
835 impaired HSP 90-dependent protein folding are hallmarks of aneuploid human cells.
836 EMBO J 2014;33:2374–87.
837
- 838 3. Gonçalves E, Fragoulis A, Garcia-Alonso L, Cramer T, Saez-Rodriguez J, Beltrao P.
839 Widespread Post-transcriptional Attenuation of Genomic Copy-Number Variation in
840 Cancer. Cell Syst 2017;5:386.
841
- 842 4. Schukken KM, Sheltzer J. Extensive protein dosage compensation in aneuploid human
843 cancers. Genome Res 2022;gr.276378.121.
844
- 845 5. Senger G, Santaguida S, Schaefer MH. Regulation of protein complex partners as a
846 compensatory mechanism in aneuploid tumors. Elife 2022;11:e75526.
847
- 848 6. Cheng P, Zhao X, Katsnelson L, Camacho-Hernandez EM, Mermerian A, Mays JC, et al.
849 Proteogenomic analysis of cancer aneuploidy and normal tissues reveals divergent modes
850 of gene regulation across cellular pathways. Elife 2022;11:e75227.
851
- 852 7. Torres EM, Sokolsky T, Tucker CM, Chan LY, Boselli M, Dunham MJ, et al. Effects of
853 aneuploidy on cellular physiology and cell division in haploid yeast. Science
854 2007;317:916–24.
855
- 856 8. Torres EM, Dephoure N, Panneerselvam A, Tucker CM, Whittaker CA, Gygi SP, et al.
857 Identification of aneuploidy-tolerating mutations. Cell 2010;143:71–83.
858
- 859 9. Dephoure N, Hwang S, O’Sullivan C, Dodgson SE, Gygi SP, Amon A, et al. Quantitative
860 proteomic analysis reveals posttranslational responses to aneuploidy in yeast. Elife
861 2014;3:e03023.
862
- 863 10. Oromendia AB, Dodgson SE, Amon A. Aneuploidy causes proteotoxic stress in yeast.
864 Genes Dev 2012; 26:2696–708.
865
- 866 11. Pavelka N, Rancati G, Zhu J, Bradford WD, Saraf A, Florens L, et al. Aneuploidy confers
867 quantitative proteome changes and phenotypic variation in budding yeast. Nature
868 2010;468:321–5.
869
- 870 12. Torres EM, Springer M, Amon A. No current evidence for widespread dosage
871 compensation in *S. cerevisiae*. Elife 2016;5:e10996.
872
- 873 13. Mohanty V, Wang F, Mills GB, Chen K. Uncoupling of gene expression from copy
874 number presents therapeutic opportunities in aneuploid cancers. Cell Rep Med
875 2021;2:100349.
876

- 877 14. Zerbib J, Ippolito MR, Eliezer Y, Feudis G De, Reuveni E, Kadmon AS, et al. Human
878 aneuploid cells depend on the RAF/MEK/ERK pathway for overcoming increased DNA
879 damage. *Nat Commun* 2024 Sept 9 [Epub ahead of print]; DOI 10.1038/s41467-024-
880 52176-x.
- 881 15. Santaguida S, Tighe A, D'Alise AM, Taylor SS, Musacchio A. Dissecting the role of
882 MPS1 in chromosome biorientation and the spindle checkpoint through the small
883 molecule inhibitor reversine. *J Cell Biol* 2010;190:73–87.
- 884 16. Santaguida S, Vasile E, White E, Amon A. Aneuploidy-induced cellular stresses limit
885 autophagic degradation. *Genes Dev* 2015;29:2010–21.
- 886 17. Subramanian A, Tamayo P, Mootha VK, Mukherjee S, Ebert BL, Gillette MA, et al. Gene
887 set enrichment analysis: A knowledge-based approach for interpreting genome-wide
888 expression profiles. *Proc Natl Acad Sci U S A* 2005;102:15545–50.
- 889 18. Muenzner J, Trébulle P, Agostini F, Zauber H, Messner CB, Steger M, et al. Natural
890 proteome diversity links aneuploidy tolerance to protein turnover. *Nature* 2024;630:149–
891 57.
- 892 19. Dürrbaum M, Kruse C, Nieken KJ, Habermann B, Storchová Z. The deregulated
893 microRNAome contributes to the cellular response to aneuploidy. *BMC Genomics*
894 2018;19:197.
- 895 20. Yahya G, Menges P, Amponsah PS, Ngandiri DA, Schulz D, Wallek A, et al. Sublinear
896 scaling of the cellular proteome with ploidy. *Nat Commun* 2022;13:1–13.
- 897 21. Stingele S, Stoehr G, Peplowska K, Cox J, Mann M, Storchova Z. Global analysis of
898 genome, transcriptome and proteome reveals the response to aneuploidy in human cells.
899 *Mol Syst Biol* 2012;8:608.
- 900 22. Xiong B, Yang Y, Fineis FR, Wang JP. DegNorm: Normalization of generalized transcript
901 degradation improves accuracy in RNA-seq analysis. *Genome Biol* 2019;20:1–18.
- 902 23. Tsitsiridis G, Steinkamp R, Giurgiu M, Brauner B, Fobo G, Frishman G, et al. CORUM:
903 the comprehensive resource of mammalian protein complexes–2022. *Nucleic Acids Res*
904 2023;51:D539–45.
- 905 24. Wang M, Zhang P, Zhu Y, Kong X, Zhang Z, Hu L. Assessing the activity of nonsense-
906 mediated mRNA decay in lung cancer. *BMC Med Genomics* 2017;10:1–7.
- 907 25. Nickless A, Jackson E, Marasa J, Nugent P, Mercer RW, Piwnica-Worms D, et al.
908 Intracellular calcium regulates nonsense-mediated mRNA decay. *Nat Med.* 2014;20:961–
909 6.
- 910 26. Gerbracht J V., Boehm V, Britto-Borges T, Kallabis S, Wiederstein JL, Ciriello S, et al.
911 CASC3 promotes transcriptome-wide activation of nonsense-mediated decay by the exon
912 junction complex. *Nucleic Acids Res* 2020;48:8626–44.
- 913
914
915
916
917
918
919
920
921
922
923
924

- 925
926 27. Azzalin CM, Reichenbach P, Khoriauli L, Giulotto E, Lingner J. Telomeric repeat-
927 containing RNA and RNA surveillance factors at mammalian chromosome ends. *Science*
928 2007;318:798–801.
929
- 930 28. Brumbaugh KM, Otterness DM, Geisen C, Oliveira V, Brognard J, Li X, et al. The mRNA
931 Surveillance Protein hSMG-1 Functions in Genotoxic Stress Response Pathways in
932 Mammalian Cells. *Mol Cell* 2004;14:585–98.
933
- 934 29. Melamed Z, Levy A, Ashwal-Fluss R, Lev-Maor G, Mekahel K, Atias N, et al.
935 Alternative Splicing Regulates Biogenesis of miRNAs Located across Exon-Intron
936 Junctions. *Mol Cell* 2013;50:869–81.
937
- 938 30. Ohashi A, Ohori M, Iwai K, Nakayama Y, Nambu T, Morishita D, et al. Aneuploidy
939 generates proteotoxic stress and DNA damage concurrently with p53-mediated post-
940 mitotic apoptosis in SAC-impaired cells. *Nat Commun* 2015;6:1–16.
941
- 942 31. Ben-David U, Amon A. Context is everything: aneuploidy in cancer. *Nat Rev Genet*
943 2020;21:44–62.
944
- 945 32. Zhu J, Tsai HJ, Gordon MR, Li R. Cellular Stress Associated with Aneuploidy. *Dev Cell*
946 2018;44:420–31.
947
- 948 33. Hetz C, Zhang K, Kaufman RJ. Mechanisms, regulation and functions of the unfolded
949 protein response. *Nat Rev Mol Cell Biol* 2020;21:421–38.
950
- 951 34. Kuznetsova AY, Seget K, Moeller GK, de Pagter MS, de Roos JADM, Dürrbaum M, et al.
952 Chromosomal instability, tolerance of mitotic errors and multidrug resistance are
953 promoted by tetraploidization in human cells. *Cell Cycle* 2015;14:2810–20.
954
- 955 35. Schmidt EK, Clavarino G, Ceppi M, Pierre P. SUnSET, a nonradioactive method to
956 monitor protein synthesis. *Nat Methods* 2009;6:275–7.
957
- 958 36. Xian S, Dosset M, Almanza G, Searles S, Sahani P, Waller TC, et al. The unfolded protein
959 response links tumor aneuploidy to local immune dysregulation. *EMBO Rep* 2021;22:
960 e52509.
961
- 962 37. Santaguida S, Amon A. Short- and long-term effects of chromosome mis-segregation and
963 aneuploidy. *Nat Rev Mol Cell Biol* 2015;16:473–85.
964
- 965 38. Cohen-Sharir Y, McFarland JM, Abdusamad M, Marquis C, Bernhard S V., Kazachkova
966 M, et al. Aneuploidy renders cancer cells vulnerable to mitotic checkpoint inhibition.
967 *Nature* 2021;590:486–91.
968
- 969 39. Corsello SM, Nagari RT, Spangler RD, Rossen J, Kocak M, Bryan JG, et al. Discovering
970 the anticancer potential of non-oncology drugs by systematic viability profiling. *Nat*
971 *Cancer* 2020;1:235–48.
972

- 973 40. Ben-David U, Mayshar Y, Benvenisty N. Virtual karyotyping of pluripotent stem cells on
974 the basis of their global gene expression profiles. *Nat Protoc* 2013;8:989–97.
975
- 976 41. Bollen S, Leddin M, Andrade-Navarro MA, Mah N. CAFE: an R package for the
977 detection of gross chromosomal abnormalities from gene expression microarray data.
978 *Bioinformatics* 2014;30:1484–5.
979
- 980 42. Mulligan G, Mitsiades C, Bryant B, Zhan F, Chng WJ, Roels S, et al. Gene expression
981 profiling and correlation with outcome in clinical trials of the proteasome inhibitor
982 bortezomib. *Blood* 2007;109:3177–88.
983
- 984 43. Borisov N, Sergeeva A, Suntsova M, Raevskiy M, Gaifullin N, Mendeleeva L, et al.
985 Machine Learning Applicability for Classification of PAD/VCD Chemotherapy Response
986 Using 53 Multiple Myeloma RNA Sequencing Profiles. *Front Oncol* 2021;11:652063.
987
- 988 44. Terragna C, Remondini D, Martello M, Zamagni E, Pantani L, Patriarca F, et al. The
989 genetic and genomic background of multiple myeloma patients achieving complete
990 response after induction therapy with bortezomib, thalidomide and dexamethasone (VTD).
991 *Oncotarget* 2015;7:9666–79.
992
- 993 45. Fraunhoffer NA, Abuelafia AM, Bigonnet M, Gayet O, Roques J, Telle E, et al.
994 Evidencing a pancreatic ductal adenocarcinoma subpopulation sensitive to the proteasome
995 inhibitor carfilzomib. *Clin Cancer Res* 2020;26:5506–19.
996
- 997 46. Stewart E, Federico SM, Chen X, Shelat AA, Bradley C, Gordon B, et al. Orthotopic
998 patient-derived xenografts of paediatric solid tumours. *Nature* 2017;549:96–100.
999
- 1000 47. Torres EM, Williams BR, Amon A. Aneuploidy: Cells losing their balance. *Genetics*
1001 2008;179:737–46.
1002
- 1003 48. Hwang S, Cavaliere P, Li R, Zhu LJ, Dephoure N, Torres EM. Consequences of
1004 aneuploidy in human fibroblasts with trisomy 21. *Proc Natl Acad Sci U S A* 2021;118:
1005 e2014723118.
1006
- 1007 49. Passerini V, Ozeri-Galai E, De Pagter MS, Donnelly N, Schmalbrock S, Kloosterman WP,
1008 et al. The presence of extra chromosomes leads to genomic instability. *Nat Commun*
1009 2016; 7:1–12.
1010
- 1011 50. Chunduri NK, Menges P, Zhang X, Wieland A, Gotsmann VL, Mardin BR, et al. Systems
1012 approaches identify the consequences of monosomy in somatic human cells. *Nat Commun*
1013 2021;12:1–17.
1014
- 1015 51. Love MI, Huber W, Anders S. Moderated estimation of fold change and dispersion for
1016 RNA-seq data with DESeq2. *Genome Biol* 2014;15:1–21.
1017
- 1018 52. Tapial J, Ha KCH, Sterne-Weiler T, Gohr A, Braunschweig U, Hermoso-Pulido A, et al.
1019 An atlas of alternative splicing profiles and functional associations reveals new regulatory

- 1020 programs and genes that simultaneously express multiple major isoforms. *Genome Res*
1021 2017;27:1759–68.
- 1022
- 1023 53. Demichev V, Messner CB, Vernardis SI, Lilley KS, Ralser M. DIA-NN: neural networks
1024 and interference correction enable deep proteome coverage in high throughput. *Nat*
1025 *Methods* 2020;17:41–4.
- 1026
- 1027 54. Bateman A, Martin MJ, Orchard S, Magrane M, Agivetova R, Ahmad S, et al. UniProt:
1028 the universal protein knowledgebase in 2021. *Nucleic Acids Res* 2021;49:D480–9.
- 1029
- 1030 55. Tsherniak A, Vazquez F, Montgomery PG, Weir BA, Kryukov G, Cowley GS, et al.
1031 Defining a Cancer Dependency Map. *Cell* 2017;170:564-576.e16.
- 1032
- 1033 56. Taylor AM, Shih J, Ha G, Gao GF, Zhang X, Berger AC, et al. Genomic and Functional
1034 Approaches to Understanding Cancer Aneuploidy. *Cancer Cell* 2018;33:676-689.e3.
- 1035
- 1036 57. Liberzon A, Birger C, Thorvaldsdóttir H, Ghandi M, Mesirov JP, Tamayo P. The
1037 Molecular Signatures Database (MSigDB) hallmark gene set collection. *Cell Syst*
1038 2015;1:417.
- 1039
- 1040 58. Colaprico A, Silva TC, Olsen C, Garofano L, Cava C, Garolini D, et al. TCGAAbiolinks: an
1041 R/Bioconductor package for integrative analysis of TCGA data. *Nucleic Acids Res*
1042 2016;44:e71.
- 1043
- 1044 59. Bray NL, Pimentel H, Melsted P, Pachter L. Near-optimal probabilistic RNA-seq
1045 quantification. *Nat Biotechnol* 2016;34:525–7.
- 1046
- 1047 60. Talevich E, Shain AH, Botton T, Bastian BC. CNVkit: Genome-Wide Copy Number
1048 Detection and Visualization from Targeted DNA Sequencing. *PLoS Comput Biol*
1049 2016;12:e1004873.
- 1050
- 1051 61. Mayrhofer M, Viklund B, Isaksson A. Rawcopy: Improved copy number analysis with
1052 Affymetrix arrays. *Sci Rep* 2016;6:1–10.
- 1053
- 1054 62. Spurr LF, Touat M, Taylor AM, Dubuc AM, Shih J, Meredith DM, et al. Quantification of
1055 aneuploidy in targeted sequencing data using ASCETS. *Bioinformatics* 2021;37:2461–3.
- 1056
- 1057 63. Chen X, Gupta P, Wang J, Nakitandwe J, Roberts K, Dalton JD, et al. CONSERTING:
1058 integrating copy number analysis with structural variation detection. *Nat Methods*
1059 2015;12:527.
- 1060
- 1061

1062 **Main Figure Legends**

1063 **Figure 1: Dosage compensation in trisomic cells occurs at both mRNA and protein levels**

1064 (a) Schematic representation of clone generation. See Zerbib *et al* (14) for more details. (b) Comparison
1065 of the differential gene expression patterns (pre-ranked GSEA results) between the pseudo-diploid SS48
1066 clone (control) and the highly-aneuploid SS51 and SS111 clones. Plot presents enrichments for the
1067 Hallmark, KEGG, Biocarta and Reactome gene sets. Transcriptomic data are obtained from Zerbib *et al*
1068 (14). Significance threshold set at $qvalue=0.25$. Enriched pathways are color-coded. (c) Comparison of
1069 the differential protein expression pattern (GSEA results) between pseudo-diploid clones SS48 and SS31,
1070 and aneuploid clones SS6, SS119, SS51 and SS111. Plot presents enrichment for Hallmark, KEGG,
1071 Reactome gene sets. Proteomics data are obtained from Zerbib *et al* (14). Significance threshold set at
1072 $qvalue=0.25$. Enriched pathways are color-coded. (d) Density plots of the mRNA expression from diploid
1073 (blue) or gained (red) chromosomes, relative to the mean expression from the genes on diploid
1074 chromosomes. The black dashed line indicates the predicted amount of mRNA from gained chromosomes
1075 in the absence of compensation. Transcriptomic data are obtained from Zerbib *et al* (14); p -value
1076 <0.0001 , two-tailed Mann-Whitney test. (e) Density plots of the protein expression from diploid (blue)
1077 or gained (red) chromosomes. The black dashed line indicates the predicted amount of protein in the
1078 absence of compensation. Proteomics data are obtained from Zerbib *et al*(14); p -value < 0.0001 , two-
1079 tailed Mann-Whitney test. (f) Comparison of the correlation between the DNA copy number levels and
1080 the mRNA and protein expression levels (in purple and orange, respectively). Correlations values
1081 obtained from the median values of the density plots. Black dotted line represents the expected correlation
1082 in the absence of dosage compensation. The correlations are below those expected without compensation,
1083 and the correlation of the protein levels to DNA copy number is lower than that of the mRNA levels. The
1084 30% most lowly-expressed transcripts/proteins were removed from the analysis to reduce noise. (g)
1085 Density plots of the protein expression from gained chromosomes, comparing those that are not part of
1086 CORUM protein complexes (grey) to those that are part of CORUM protein complexes (red). The black
1087 dashed line indicates the predicted protein expression in the absence of compensation. Expression values
1088 are normalized to those from the proteins encoded from diploid chromosomes; p -value < 0.0001 , two-
1089 tailed Mann-Whitney test. (h) Comparison of the differential gene dependency scores (pre-ranked GSEA
1090 results) between the near-diploid SS48 clone (control) and the aneuploid SS6, SS119 and SS51 clones.
1091 Plot presents enrichments for the Hallmark, KEGG, Biocarta and Reactome gene sets. Data are obtained
1092 from Zerbib, Ippolito *et al*¹⁶. Significance threshold set at $qvalue=0.25$. Enriched pathways are color-
1093 coded.

1094
1095 **Figure 2: Trisomic cells compensate for the extra DNA content through increased RNA**
1096 **and protein turn-over**

1097 (a) Immunofluorescence of nascent RNA foci in pseudo-diploid clones, SS48 and SS31, and in highly-
1098 aneuploid clones, SS51 and SS111. Red, nascent RNA; Blue, DAPI; Scale bar, 10 μ m. (b) Quantitative
1099 comparison of nascent RNA showing area (pixel) of nascent RNA foci. $n=3$ independent experiments;
1100 ****, $p<0.0001$; Kruskal–Wallis test, Dunn’s multiple comparison. (c) Quantification of total RNA
1101 between pseudo-diploid clones (SS48 and SS31) and highly-aneuploid clones (SS51 and SS111). $n=7$
1102 independent experiments; RNA content was calculated relative to SS48, per experiment. **, $p=0.007$ and
1103 $p=0.0018$, for SS51 and SS111 respectively; One-Sample t-test. (d) Immunofluorescence of nascent RNA
1104 foci in pseudo-diploid RPE1-hTERT treated with DMSO or after 72hrs following reversine pulse. Red,
1105 nascent RNA; Blue, DAPI; Scale bar, 10 μ m. (e) Quantitative comparison of nascent RNA showing area
1106 (pixel) of nascent RNA foci. $n=3$ independent experiments; ****, $p<0.0001$; two-tailed Mann-Whitney

1107 test. **(f)** Gene set enrichment analysis (GSEA) of an RNA catabolism gene expression signature,
1108 comparing the highly-aneuploid clones, SS51 and SS111, to the pseudo-diploid clone SS48. Data are
1109 obtained from Zerbib *et al* (14). Shown is an enrichment plot for the GO Biological Process ‘Negative
1110 regulation of RNA catabolic processes’ gene set (NES= -1.58; q-value=0.2). **(g)** Comparison of the mean
1111 degradation index (degraded RNA score) across all genes (n=13,689), using the Degnorm algorithm.
1112 Median DI score: 0.33 (SS48), 0.4 (SS51) and 0.38 (SS111). ****, p<0.0001; Repeated-Measured One-
1113 Way ANOVA, Tukey’s multiple comparison test. **(h)** Native agarose gel electrophoresis of total RNA
1114 extracted from RPE1 clones, re-suspended in Nuclease-Free water, showing a specific increased amount
1115 of RNA smear in the highly-aneuploid clones, SS51 and SS111, in comparison to the pseudo-diploid
1116 clones SS48 and SS31. **(i)** Quantification of RNA degradation, as evaluated by the smear/total RNA ratio.
1117 Fold change in normalized smear was calculated relative to SS48, per experiment. n=4 independent
1118 experiments; *, p=0.0102 and p=0.034, for SS51 and SS111, respectively; One-Sample t-test. **(j)** cJUN
1119 mRNA expression levels 30min following actinomycin D treatment, showing increased RNA degradation
1120 rate in the highly-aneuploid clones. mRNA expression was normalized to the respective vehicle-treated
1121 control. n=4 independent experiments. **, p=0.0024 for pseudo-diploid (SS48 and SS31) vs highly
1122 aneuploid clones (SS51 and SS111); two-tailed unpaired t-test. **(k)** Density plots of the RNA degradation
1123 index of genes that are not part of CORUM protein complexes (grey) vs. genes that are part of CORUM
1124 protein complexes (red). Degradation values are normalized to the degradation indices of the diploid
1125 chromosomes. ****p <0.0001, two-tailed Mann-Whitney test.

1126

1127 **Figure 3: Aneuploid cells activate the nonsense-mediated decay (NMD) pathway, and**
1128 **depend on this pathway for downregulating their gene expression**

1129 **(a)** Gene set enrichment analysis (GSEA) of an NMD-related signature, comparing the highly-aneuploid
1130 clones, SS51 and SS111, to the pseudo-diploid clone SS48. Shown is the enrichment plot for the GO-
1131 Biological Process ‘Nuclear transcribed mRNA catabolic processes NMD’ gene set (NES=1.83; q-
1132 value=0.07). Data are taken from Zerbib *et al* (14) **(b)** Comparison of gene expression of the NMD
1133 pathway between the highly-aneuploid clones SS51 and SS111, and the pseudo-diploid clone SS48. Fold
1134 change in transcriptional score was calculated relative to SS48, for each gene (n=43 genes). ****,
1135 p<0.0001; One-Sample t-test. Data are obtained from Zerbib *et al*(14) **(c)** The top 3,000 genes that
1136 aneuploid clones were most preferentially sensitive to their knockout in comparison to the pseudo-diploid
1137 clone SS48, based on our genome-wide CRISPR/Cas9 screen. Highlighted are genes that belong to the
1138 NMD pathway: core member genes (in pink) and ribosomal-related genes (in purple). NMD-related genes
1139 are significantly enriched within the top 3,000 gene list; ****, p<0.0001; two-tailed Fisher’s Exact test.
1140 Data are obtained from Zerbib *et al* (14) **(d)** Comparison of sensitivity (determined by EC50 values) to
1141 72hrs drug treatment with the NMD inhibitor ouabain, between pseudo-diploid clones (SS48 and SS31)
1142 and highly-aneuploid clones (SS51 and SS111). EC50 fold-change was calculated relative to SS48, per
1143 experiment. n=5 independent experiments; *, p=0.0142 and ***, p=0.0009, for SS111 and SS51,
1144 respectively; One-Sample t-test. **(e)** Comparison of CASC3 mRNA levels, quantified by qRT-PCR,
1145 between pseudo-diploid clones (SS48 and SS31) and highly-aneuploid clones (SS51 and SS111). Fold
1146 change in CASC3 expression was calculated relative to SS48, per experiment. n=5 (SS31) and n=6
1147 (SS48, SS51, SS111) independent experiments; **, p=0.0058 and p=0.0018, for SS51 and SS111,
1148 respectively; One-Sample t-test. **(f)** Comparison of cell viability following pooled siRNA against CASC3
1149 for 72hrs, between pseudo-diploid clones (SS48 and SS31) and highly aneuploid clones (SS51 and
1150 SS111). Viability was calculated relative to a control siRNA treatment. n=5 independent experiments; *,
1151 p<0.05; **, p<0.01; ****, p<0.0001; One-Way ANOVA, Tukey’s multiple comparison. All comparisons
1152 between SS31 and aneuploid clones were significant as well (*, p<0.05). **(g)** Comparison of cell viability

1153 following siRNA against CASC3, between parental RPE1 cells treated for 20hrs with the SAC inhibitor
1154 reversine (500nM) or with control DMSO, then harvested 72hrs post wash-out. Relative viability was
1155 calculated relative to a control siRNA treatment. n=4 independent experiments; *, p=0.0425; two-tailed
1156 paired t-test. **(h)** Comparison of cell viability following siRNA against CASC3 in additional pseudo-
1157 diploid non-transformed cell lines (BJ-hTERT and IMR90), treated for 36hrs with the SAC inhibitor
1158 reversine (500nM) or with control DMSO, then harvested 72hrs post wash-out. Relative viability was
1159 calculated relative to control siRNA treatment. n=7 (BJ-hTERT) and n=6 (IMR90) independent
1160 experiment. ***, p=0.0006 and p=0.0004 for BJ-hTERT and IMR90 respectively; one-tailed paired t-test.
1161 **(i)** Comparison of cell viability following siRNA against CASC3 in additional pseudo-diploid cancer cell
1162 lines (CAL51, HCT116, and SW48), treated for 24hrs with the SAC inhibitor reversine (125nM for
1163 CAL51 and HCT116, 200nM for SW48) or with control DMSO, then harvested 72hrs post wash-out.
1164 Relative viability was calculated relative to control siRNA treatment. n=9 (CAL51), n=7 (HCT116) and
1165 n=6 (SW48) independent experiment. *, p=0.0114 for SW48, **, p=0.0061 and p=0.0084 for CAL51 and
1166 HCT116 respectively; one-tailed paired t-test. **(j)** Gene set enrichment analysis of the genes whose
1167 expression correlates with proliferation in highly-aneuploid cancer cell lines but not in near-diploid
1168 cancer cell lines, reveals significant enrichment of multiple RNA metabolism signatures. Shown here are
1169 the Reactome ‘Metabolism of RNA’ and ‘Nonsense Mediated Decay’ gene sets. Significance values
1170 represent the FDR q-values. The ranking of each RNA metabolism signature (out of all signatures
1171 included in the gene set collection) is indicated next to each bar. **(k-l)** Comparison of gene dependency
1172 (determined by Chronos score) for key members of the NMD pathway, the EJC member CASC3 **(k)** and
1173 the main effector UPF1 **(l)**, between the top and bottom aneuploidy quartiles of human cancer cell lines
1174 (n=538 cell lines). Data were obtained from DepMap CRISPR screen, 22Q1 release. *, p=0.0289 and
1175 ****, p<0.0001, for CASC3 and UPF1 respectively; two-tailed Mann-Whitney test. **(m)** Comparison of
1176 cell viability following siRNA against CASC3 in three representative pseudo-diploid cancer cell lines
1177 (CAL51, HCT116, and SW48) vs. three representative highly-aneuploid cancer cell lines (MDA-MB-468,
1178 A101D, SH10TC), harvested 72hrs post wash-out. Viability was calculated relative to control siRNA
1179 treatment. n=5 (CAL51, HCT116) and n=6 (SW48, MDA-MB-468, A101D, SH10TC) independent
1180 experiment. ***, p=0.0049 for lowly- vs. highly-aneuploid cell lines ; one-tailed unpaired t-test,
1181 comparing the mean value of each cell line. **(n)** Pre-ranked GSEA of mRNA expression levels showing
1182 that high aneuploidy levels are associated with upregulation of the nonsense-mediated decay (NMD) in
1183 human primary tumors. Shown is the GO-Biological Process ‘Nuclear transcribed mRNA catabolic
1184 processes NMD’ gene set (NES=1.70, q-value=0.029) gene set. Data were obtained from the TCGA
1185 mRNA expression data set(58).

1186
1187 **Figure 4: Aneuploid cells activate the miRNA pathway, and depend on this pathway for**
1188 **downregulating their gene expression**

1189 **(a)** Gene set enrichment analysis (GSEA) of miRNA-related signatures, comparing the highly-aneuploid
1190 clones, SS51 and SS111, to the pseudo-diploid clone SS48. Shown are enrichment plots for the Reactome
1191 ‘Transcriptional regulation by small RNAs’ (NES=2.64; q-value<0.0001) and the Reactome ‘Gene
1192 silencing by RNA’ (NES=2.36; q-value=0.00016) gene sets. Data are obtained from Zerbib *et al* (14) **(b)**
1193 Venn diagram of the overlap between downregulated mRNAs (in grey) and upregulated miRNAs (in
1194 pink) in highly-aneuploid clones (SS51 and SS111) vs. pseudo-diploid clones (SS48 for the mRNA and
1195 SS48/SS31 for the miRNA). ****, p<0.0001, one-sided chi-squared test **(c)** The top 3,000 genes that
1196 aneuploid clones were most preferentially sensitive to their knockout in comparison to the pseudo-diploid
1197 clone SS48, based on our genome-wide CRISPR/Cas9 screen. Highlighted are genes that belong to the
1198 miRNA biogenesis pathway (in pink), based on the Reactome ‘miRNA biogenesis’ signature (RNA

1199 polymerase II genes excluded). miRNA genes are significantly enriched within the top 3,000 gene list. **,
1200 $p=0.0064$; two-tailed Fisher's Exact test. Data are obtained from Zerbib *et al*(14) **(d)** Comparison of
1201 DROSHA mRNA levels, quantified by qRT-PCR, between pseudo-diploid clones (SS48 and SS31) and
1202 highly-aneuploid clones (SS51 and SS111). Fold change in DROSHA expression was calculated relative
1203 to SS48, per experiment. $n=4$ independent experiments; *, $p=0.0325$ and **, $p=0.0079$, for SS51 and
1204 SS111, respectively; One-Sample t-test. **(e)** Comparison of cell viability following siRNA against
1205 DROSHA for 72hrs, between pseudo-diploid clones (SS48 and SS31) and highly-aneuploid clones (SS51
1206 and SS111). Viability was calculated relative to control siRNA. $n=5$ independent experiments; *,
1207 $p=0.0425$ (SS48/SS51) and $p=0.0148$ (SS48/SS111); One-Way ANOVA, Tukey's multiple comparison
1208 test. All comparisons between SS31 and aneuploid clones were significant as well (**, $p<0.01$). **(f)**
1209 Comparison of cell viability following siRNA against DROSHA in additional pseudo-diploid non-
1210 transformed cell lines (BJ-hTERT and IMR90), treated for 36hrs with the SAC inhibitor reversine
1211 (500nM) or with control DMSO, then harvested 72hrs post wash-out. Viability was calculated relative to
1212 control siRNA treatment. $n=6$ (BJ-hTERT) and $n=7$ (IMR90) independent experiments. **, $p=0.0027$ and
1213 **** $p<0.0001$ for BJ-hTERT and IMR90 respectively; one-tailed paired t-test. **(g)** Comparison of cell
1214 viability following siRNA against DROSHA in additional pseudo-diploid cancer cell lines (CAL51,
1215 HCT116, and SW48), treated for 24hrs with the SAC inhibitor reversine (125nM for CAL51 and
1216 HCT116, 200nM for SW48) or with control DMSO, then harvested 72hrs post wash-out. Viability was
1217 calculated relative to control siRNA treatment. $n=6$ (CAL51), $n=5$ (HCT116 and SW48) independent
1218 experiments. **, $p=0.0073$ $p=0.0024$ and $p=0.0069$ for CAL51, HCT116 and SW48, respectively; one-
1219 tailed paired t-test. **(h)** Comparison of DROSHA mRNA expression levels between the top and bottom
1220 aneuploidy quartiles of human cancer cell lines ($n=738$ cell lines). Data were obtained from the DepMap
1221 Expression 22Q1 release. DROSHA mRNA expression is significantly higher in highly aneuploid cancer
1222 cell lines. ****, $p<0.0001$; two-tailed Mann-Whitney test. **(i)** Comparison of cell viability following
1223 siRNA against DROSHA in three representative pseudo-diploid cancer cell lines (CAL51, HCT116, and
1224 SW48) vs. three representative highly-aneuploid cancer cell lines (MDA-MB-468, A101D, SH10TC),
1225 harvested 72hrs post wash-out. Viability was calculated relative to control siRNA treatment. $n=6$
1226 independent experiments. *, $p=0.0129$ for lowly- vs. highly-aneuploid cell lines; one-tailed unpaired t-
1227 test, comparing the mean value of each cell lines. **(j)** Pre-ranked GSEA of mRNA expression levels
1228 showing that high aneuploidy levels are associated with upregulation of gene silencing in human primary
1229 tumors. Shown are the Reactome 'Transcriptional regulation by small RNAs' (NES=1.98; q -value=0.001)
1230 and the Reactome 'Gene silencing by RNA' (NES=1.86; q -value=0.004) gene sets. Data were obtained
1231 from the TCGA mRNA expression data set(58).
1232

1233 **Figure 5: Aneuploid cells experience proteotoxic stress and attenuate protein translation**

1234 **(a)** Gene set enrichment analysis (GSEA) of proteotoxic stress-related signatures, comparing the highly-
1235 aneuploid clones, SS51 and SS111, to the pseudo-diploid clone SS48. Shown are the enrichment plots for
1236 the Reactome gene sets 'IRE1a activates chaperones' (NES=1.77; q -value=0.022), 'Protein folding'
1237 (NES=1.55, q -value=0.084), and 'Ub-specific processing proteases' (NES=1.67, q -value=0.041). Data are
1238 obtained from Zerbib *et al* (14) **(b)** Comparison of UPR mRNA levels, quantified by qRT-PCR, between
1239 pseudo-diploid (SS48 and SS31) and highly aneuploid clones (SS51 and SS111). The expression levels of
1240 the following canonical members of the UPR were measured: XBP1-spliced/XBP1-unspliced ratio and
1241 EDEM1 (IRE1a pathway), GRP78 (ATF6 pathway) and CHOP (PERK pathway). Fold change in
1242 expression was calculated relative to SS48, per experiment. $n=6$ (XBP1 ratio, EDEM1) or $n=5$ (GRP78,
1243 CHOP) independent experiments. XBP1 ratio: *, $p=0.0194$, **, $p=0.0035$ and ***, $p=0.0005$ for SS31,
1244 SS111, and SS51, respectively EDEM1: *, $p=0.0382$ and **, $p=0.0015$ and $p=0.0052$ for SS31, SS51 and

1245 SS111, respectively. GRP78: **, $p=0.0043$ and ****, $p<0.0001$ for SS51 and SS111, respectively.
1246 CHOP: *, $p=0.0197$ and **, $p=0.0095$ for SS111 and SS51, respectively; One-Sample t-test. **(c)** Western
1247 blots of GRP78, PERK and ATF4 protein levels in pseudo-diploid clones (SS48 and SS31) and highly-
1248 aneuploid clones (SS51 and SS111). β -Actin and GAPDH were used as housekeeping controls. **(d)**
1249 Quantification of GRP78, PERK and ATF4 protein levels, calculated relative to SS48 per experiment.
1250 GRP78 (n=11 independent experiments): *, $p=0.00193$ and **, $p=0.0019$ for SS51 and SS111 respectively;
1251 PERK (n=8 independent experiments): *, $p=0.0245$ and ****, $p=0.0005$ for SS51 and SS111, ATF4 (n=7
1252 independent experiments): *, $p=0.0122$ and **, $p=0.0041$ for SS51 and SS111 respectively; One Sample
1253 t-test. **(e)** Comparison of drug sensitivity (determined by EC50 values) to 48hr treatment with the UPR
1254 activator tunicamycin, between pseudo-diploid clones (SS48 and SS31) and highly-aneuploid clones
1255 (SS51 and SS111). EC50 fold-change was calculated relative to SS48, per experiment. n=4 independent
1256 experiments; *, $p=0.004$ and **, $p=0.0079$, for SS51 and SS111, respectively; One-Sample t-test. **(f)**
1257 Comparison of drug sensitivity (determined by EC50 values) to 48hr treatment with the UPR activator
1258 tunicamycin, between parental RPE1 cells treated for 20hrs with the SAC inhibitor reversine (500nM) or
1259 with control DMSO. n=5 independent experiments. EC50 fold-change was calculated relative to RPE1-
1260 DMSO cells, per experiment. **, $p=0.0017$; One-Sample t-test **(g)** Comparison of drug sensitivity
1261 (determined by EC50 values) to 48hrs treatment with UPR activator tunicamycin, in additional non-
1262 transformed cell lines (BJ-hTERT and IMR90) treated for 36hrs with the SAC inhibitor reversine
1263 (500nM) or with control DMSO. n=6 independent experiments; *, $p=0.0223$ and $p=0.0105$ for BJ-hTERT
1264 and IMR90, respectively, one-tailed paired t-test. **(h)** Comparison of drug sensitivity (determined by
1265 EC50 values) to 48hrs treatment with UPR activator tunicamycin, in additional near-diploid cancer cell
1266 lines (CAL51, HCT116, SW48) treated for 24hrs with the SAC inhibitor reversine (125nM for CAL51
1267 and HCT116, 200nM for SW48) or with control DMSO. n=5 (CAL51) or n=4 (HCT116, SW48)
1268 independent experiments. *, $p=0.0334$ and **, $p=0.0022$ and $p=0.0094$ for CAL51, HCT116 and SW48.
1269 respectively; one-tailed paired t-test **(i)** Representative image of a SUnSET puromycin incorporation
1270 assay, showing reduction in global translation in highly-aneuploid clones (SS51 and SS111) in
1271 comparison to pseudo-diploid clones (SS48 and SS31). Vinculin was used as a housekeeping control. **(j)**
1272 Quantitative comparison of SUnSET puromycin incorporation between pseudo-diploid (SS48 and SS31)
1273 and highly-aneuploid clones (SS51 and SS111), calculated relative to SS48. n=5 independent
1274 experiments; *, $p=0.0323$ and **, $p=0.009$ for SS51 and SS111 respectively; One-Sample t-test. **(k)**
1275 Representative image of a SUnSET puromycin incorporation in parental RPE1 cells treated for 20hrs with
1276 the SAC inhibitor reversine (500nM) or with control DMSO, showing reduction in global translation
1277 following reversine-mediated aneuploidization. Vinculin was used as a housekeeping control. **(l)**
1278 Quantitative comparison of SUnSET puromycin incorporation between DMSO and reversine-treated
1279 RPE1 cells, calculated relative to DMSO-treated cells. n=6 independent experiments; **, $p=0.0012$; One-
1280 Sample t-test **(m)** Gene set enrichment analysis (GSEA) of the genes whose expression correlates with
1281 proliferation in highly-aneuploid cancer cell lines but not in near-diploid cancer cell lines, reveals
1282 significant enrichment for UPR. Shown is Hallmark 'Unfolded Protein Response'. Significance values
1283 represent the FDR q-values. The ranking of each proteasome signature (out of all signatures included in
1284 the gene set collection) is indicated next to each bar. Data were obtained from DepMap Expression 22Q1
1285 release. **(n)** Pre-ranked GSEA of mRNA expression levels showing that high aneuploidy levels are
1286 associated with upregulation of the UPR in human primary tumors. Shown is the Hallmark 'Unfolded
1287 Protein Response' (NES=1.80, q-value=0.001) gene set. Data were obtained from the TCGA mRNA
1288 expression data set(58).
1289

1290 **Figure 6: Aneuploid cells activate the proteasome, and depend on its activity for**
1291 **downregulating their protein expression**
1292 (a) Comparison of mRNA levels, quantified by qRT-PCR, between pseudo-diploid (SS48 and SS31) and
1293 highly-aneuploid clones (SS51 and SS111) of representative subunits of the 20S and 19S proteasome
1294 complexes: PSMA1, PSMB5, PSMC1, PSMD12. Fold change in expression was calculated relative to
1295 SS48, per experiment. n=6 independent experiments; PSMA1: *, p=0.0348 and p=0.0155 for SS51 and
1296 SS111 respectively, PSMB5: *, p=0.02789, **, p=0.0064 and p=0.0032 for SS31, SS51 and SS111
1297 respectively, PSMC1: **, p=0.0045 and p=0.0057 for SS51 and SS111 respectively, PSMD12: *,
1298 p=0.0233 and **, p=0.0094 for SS111 and SS51 respectively; One-Sample t-test. (b) The levels of
1299 proteasome activity, measured by Proteasome-Glo®, in pseudo-diploid (SS48 and SS31) and highly-
1300 aneuploid clones (SS51 and SS111), showing increased proteasome activity in highly-aneuploid clones.
1301 Proteasome activity was calculated relative to SS48, per experiment. n=5 independent experiment, **,
1302 p=0.0027 and p=0.0056, for SS51 and SS111 respectively; One-Sample t-test. (c) The top 3,000 genes
1303 that aneuploid clones were most preferentially sensitive to their knockout in comparison to the pseudo-
1304 diploid clone SS48, based on our genome-wide CRISPR/Cas9 screen. Data are obtained from Zerbib *et al*
1305 (14). Highlighted are genes that belong to the proteasome complex (based on KEGG ‘Proteasome’ gene
1306 set). Proteasome genes are significantly enriched within the top 3,000 gene list; *, p=0.0233; two-tailed
1307 Fisher’s Exact test. (d) Comparison of drug sensitivity (determined by EC50 values) to 72hrs drug
1308 treatment with the proteasome inhibitor bortezomib, between pseudo-diploid clones (SS48 and SS31) and
1309 highly-aneuploid clones (SS51 and SS111). EC50 fold-change was calculated relative to SS48, per
1310 experiment. n=5 independent experiments; *, p=0.0437 and p=0.0163, for SS51 and SS111, respectively;
1311 One-Sample t-test. (e-f) Comparison of mRNA expression levels of 20S (e) and 19S (f) proteasome
1312 subunits between the top and bottom aneuploidy quartiles of human cancer cell lines (n=738 cell lines).
1313 Data were obtained from the DepMap CRISPR screen 22Q1 release. 20S and 19S mRNA expression
1314 levels are significantly increased in highly-aneuploid cancer cell lines. ****, p<0.0001; two-tailed Mann-
1315 Whitney test. (g) The levels of proteasome activity, measured by ProteasomeGlo® in three pseudo-
1316 diploid (CAL51, HCT116, SW48) and three highly-aneuploid (MDA-MB-468, A101D, SH10TC) cancer
1317 cell lines. n=4 independent experiments; *, p=0.011 for low vs. highly aneuploid cancer cells (comparison
1318 of averaged activity for each cell line); one-tailed unpaired t-test. (h) Gene set enrichment analysis
1319 (GSEA) of the genes whose expression correlates with proliferation in highly-aneuploid cancer cell lines
1320 but not in near-diploid cancer cell lines, reveals significant enrichment of proteasome-related signatures.
1321 Shown here are Biocarta ‘Proteasome’ and KEGG ‘Proteasome’ signatures. Significance values represent
1322 the FDR q-values. The ranking of each proteasome signature (out of all signatures included in the gene set
1323 collection) is indicated next to each bar. Data were obtained from DepMap Expression 22Q1 release. (i)
1324 Pre-ranked GSEA of mRNA expression levels showing that high aneuploidy levels are associated with
1325 upregulation of the proteasome in human primary tumors. Shown is the enrichment plot of KEGG
1326 ‘Proteasome’ (NES=1.65; q-value=0.042) gene set. Data were obtained from TCGA mRNA
1327 expression(58). (j-k) Comparison of gene dependency (determined by DEMETER2 score) for 20S (j) and
1328 19S (k) proteasome subunits, between the top and bottom aneuploidy quartiles of human cancer cell lines
1329 (n=738 cell lines). Data were obtained from the DepMap RNAi screen, 22Q1 release. **, p=0.0089 and *,
1330 p=0.0462 for 20S and 19S proteasome subunits, respectively; two-tailed Mann-Whitney test. (l)
1331 Comparison of drug sensitivity (determined by AUC) to the proteasome inhibitor bortezomib, between
1332 the top and bottom aneuploidy quartiles of human cancer cell lines (n=203 cell lines). Data were obtained
1333 from GDSC1 drug screen, DepMap portal 22Q1 release. *, p=0.0404; two-tailed t-test test. (m)
1334 Comparison of drug sensitivity (determined by EC50 values) after 72hrs of treatment with the proteasome
1335 inhibitor bortezomib, in additional non-transformed cell lines (BJ-hTERT and IMR90) treated for 36hrs

1336 with the SAC inhibitor reversine (500nM) or with control DMSO. n=6 (BJ-hTERT) and n=4 (IMR90)
1337 independent experiments; **, p=0.0046 and p=0.0078 for BJ-hTERT and IMR90 respectively, one-tailed
1338 paired t-test. **(n)** Comparison of drug sensitivity (determined by EC50 values) to 72hrs treatment with the
1339 proteasome inhibitor bortezomib, in additional pseudo-diploid cancer cell lines (CAL51, HCT116, SW48)
1340 treated for 24hrs with the SAC inhibitor reversine (125nM for CAL51 and HCT116, 200nM for SW48) or
1341 with control DMSO. n=5 (CAL51) or n=4 (HCT116, SW48) independent experiments. *, p=0.0122 and
1342 p=0.0179 for CAL51 and SW48, respectively; one-tailed paired t-test **(o)** Comparison of drug sensitivity
1343 (determined by EC50 values) of 5 near-euploid (CAL51, EN, MHHNB11, SW48 and VMCUB1) and 5
1344 highly-aneuploid (MDA-MB-468, NCIH1693, PANC0813, SH10TC, A101D) cancer cell lines to 72hrs
1345 drug treatment with the proteasome inhibitor bortezomib. *, p=0.0317; Mann-Whitney test. **(p)** PRISM-
1346 based(39) comparison of drug sensitivity (determined by EC50 values) to 120hrs treatment with the
1347 proteasome inhibitor bortezomib, between cancer cells treated with the SAC inhibitor reversine (250nM)
1348 or with control DMSO (n=387 cell lines). Aneuploidy induction sensitized cancer cells to bortezomib.
1349 ****, p<0.0001; two-tailed Wilcoxon rank sum test. **(q)** Comparison of the aneuploidy scores (AS) of
1350 multiple myeloma patients (IgG subtype) treated with bortezomib in monotherapy(42). Patients with a
1351 Complete Response ('responders'; n=8) have significantly higher AS in comparison to patients with a
1352 progressive disease ('non-responders'; n=50); *, p=0.014, one-tailed Mann-Whitney test. **(r)** Comparison
1353 of the aneuploidy scores (AS) of multiple myeloma patients treated with bortezomib in combination with
1354 chemotherapies and dexamethasone(43). Patients with a 'Complete Response' (n=13) have significantly
1355 higher AS in comparison to patients with a 'Minimal Response' (n=14). *, p=0.0382, one-tailed Mann-
1356 Whitney test.

1357

1358 **Figure 7: Aneuploid cells with extra chromosomes compensate for their excessive DNA**
1359 **content at both the RNA and the protein level**

1360 A summary illustration of the study. Increased DNA content leads to increased transcription in aneuploid
1361 cells, which is counterbalanced by reducing the cellular mRNA levels via activation of the NMD and the
1362 miRNA pathways. The increase in the number of total and aberrant transcripts induces accumulation of
1363 misfolded proteins that triggers the UPR. Consequently, aneuploid cells decrease their protein translation
1364 and increase their protein degradation by activating the proteasome machinery. Aneuploid cells therefore
1365 become preferentially sensitive to the perturbation of both RNA and protein metabolism.

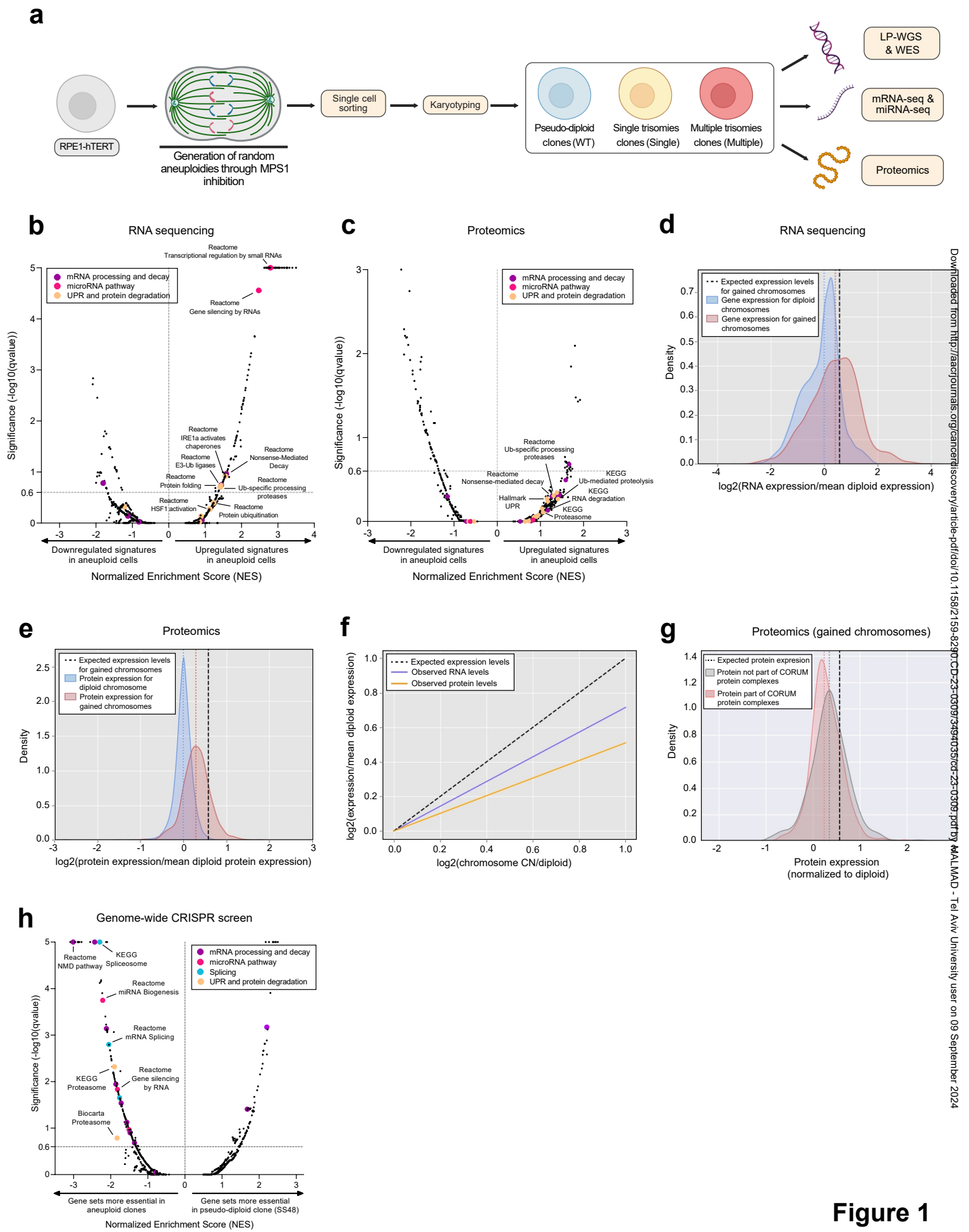


Figure 1

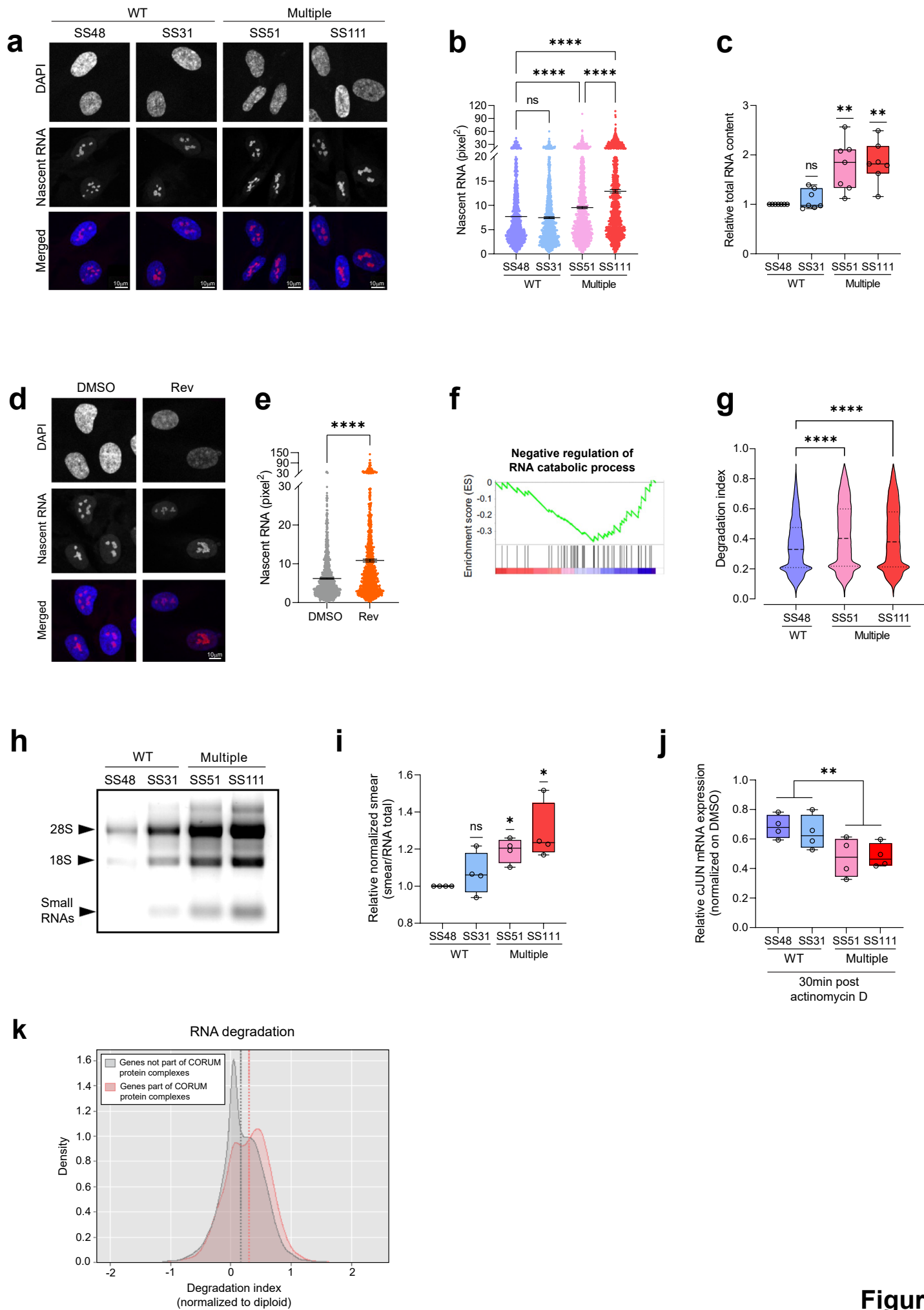


Figure 2

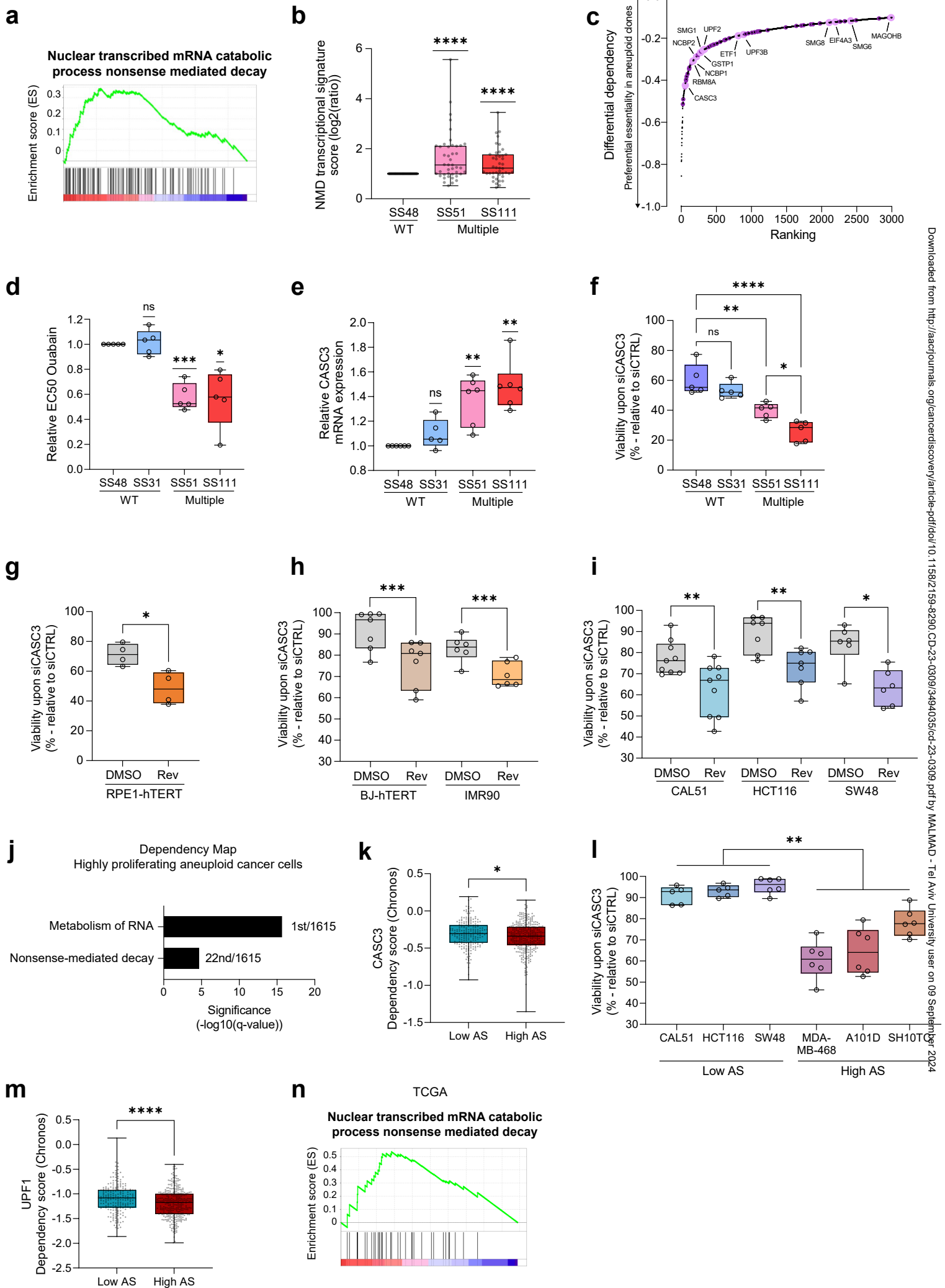


Figure 3

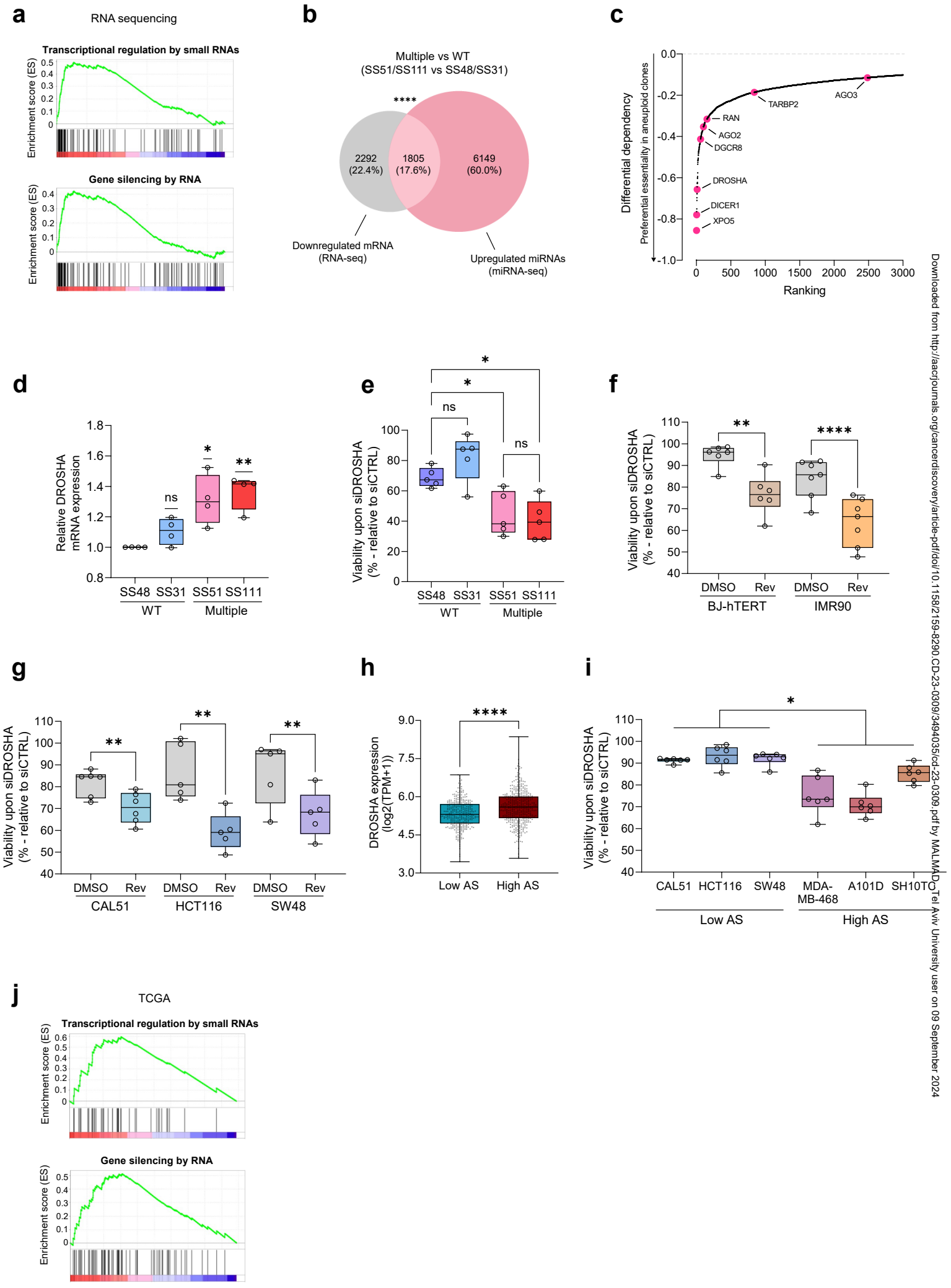


Figure 4

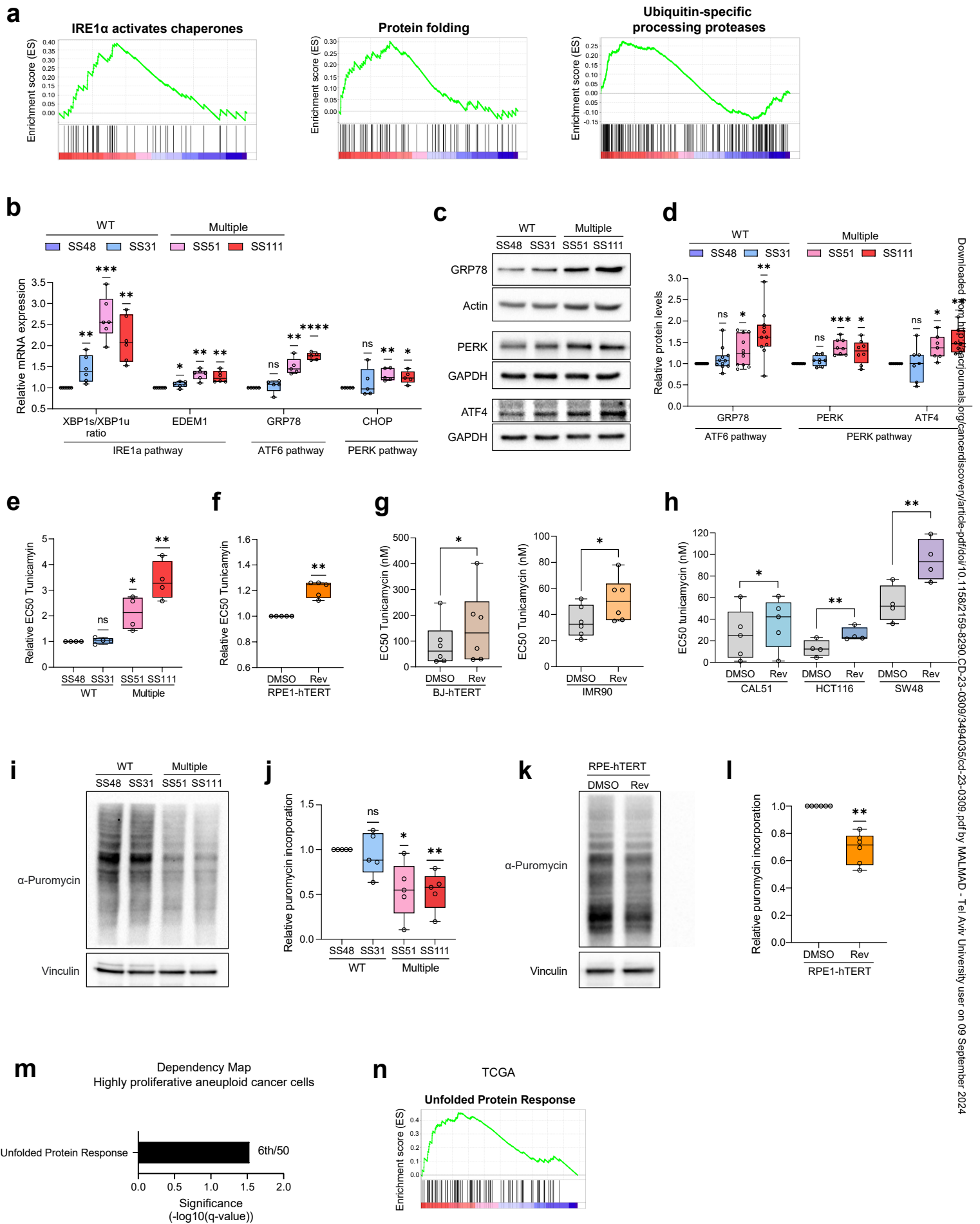


Figure 5

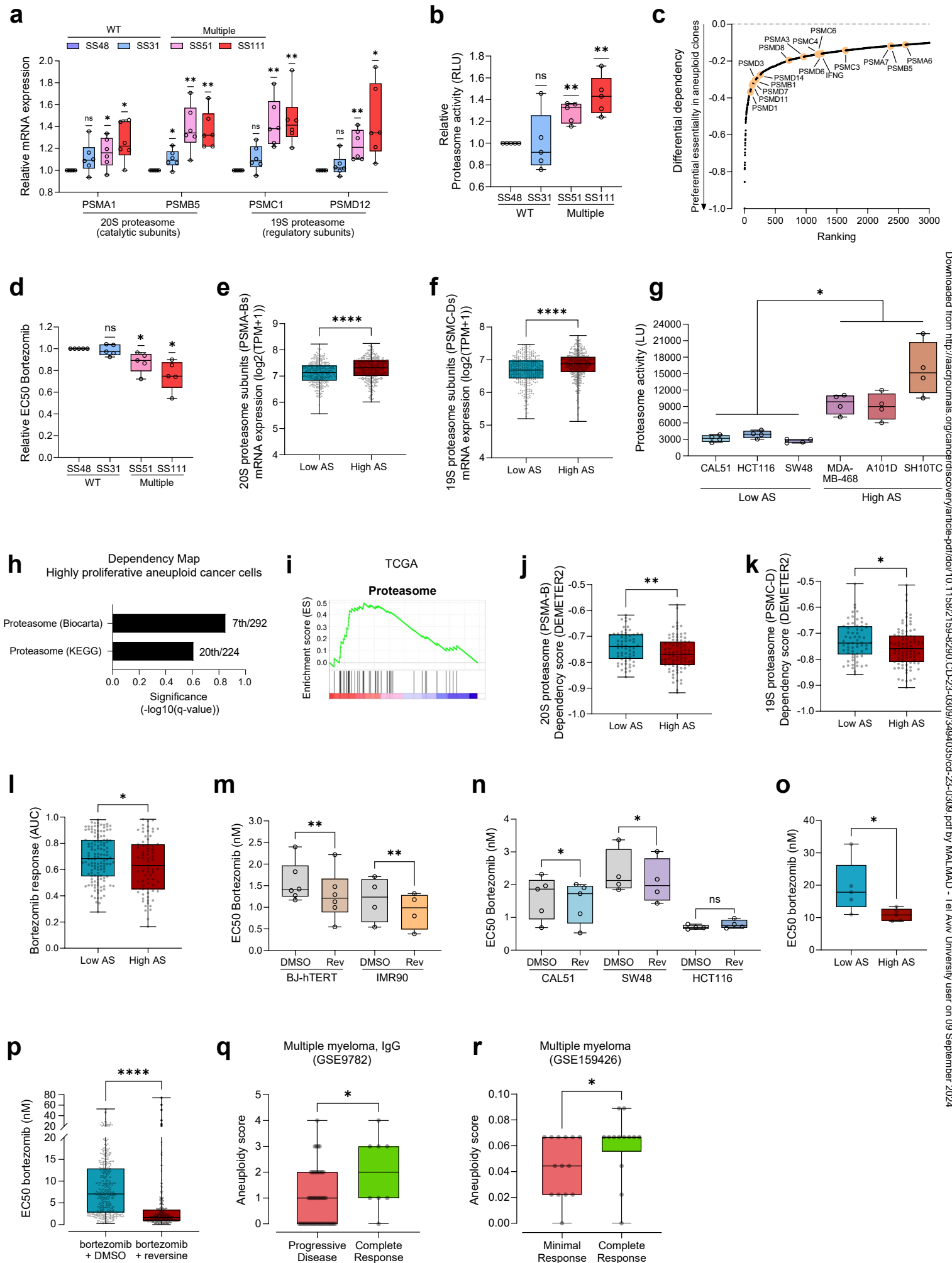


Figure 6

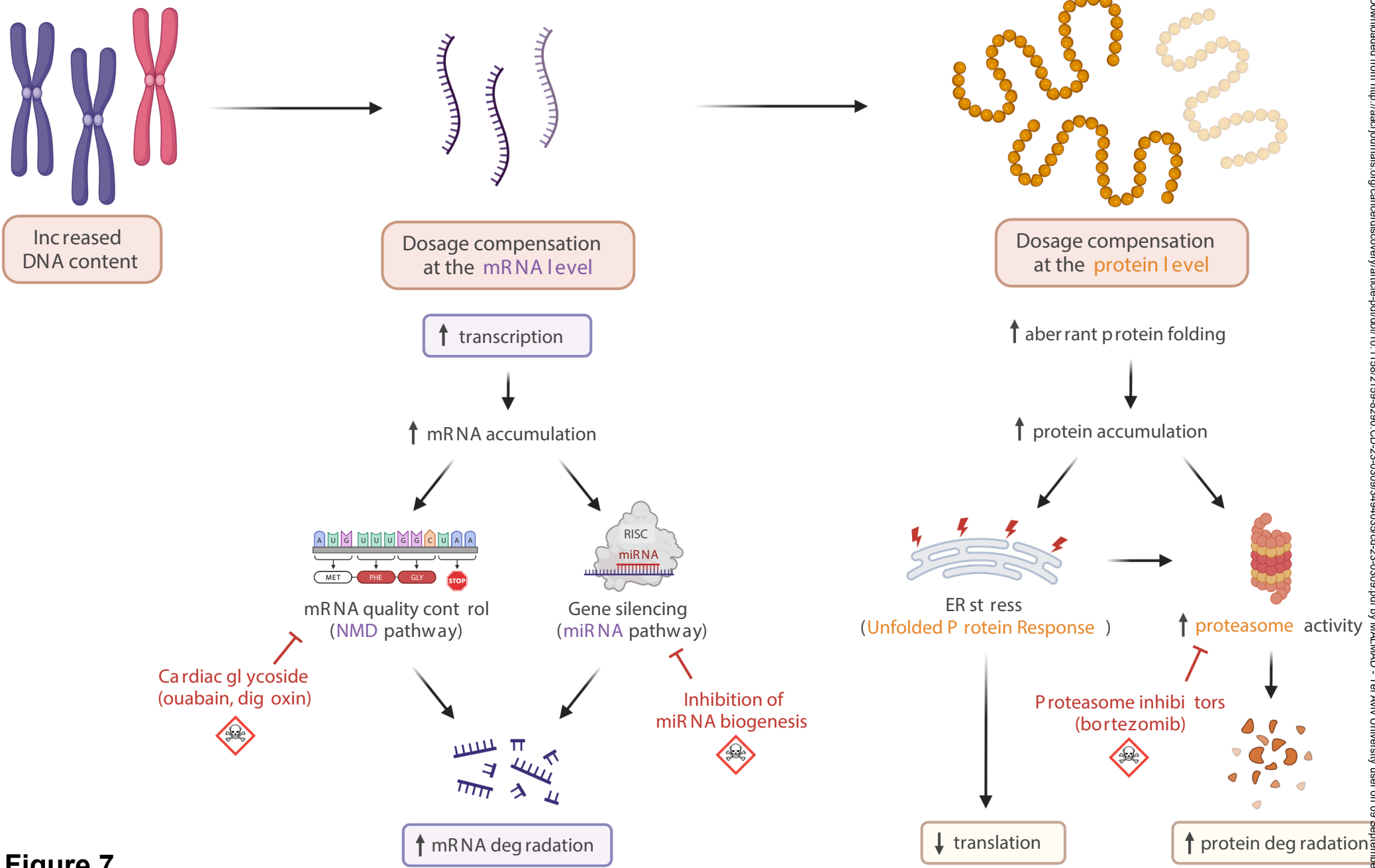


Figure 7